The gravity and topography of the terrestrial planets

Mark A. Wieczorek

Institut de Physique du Globe de Paris, France. E-mail: wieczor@ipgp.jussieu.fr

SUMMARY

This chapter reviews our current knowledge of the gravity and topography of the terrestrial planets and describes the methods that are used to analyze these data. First, a general review of the mathematical formalism that is used in describing the properties of gravitational fields and topography is given. Next, the basic properties of the gravity and topography of the Earth, Venus, Mars, and the Moon are characterized. Following this, the relationship between gravity and topography is quantified, and techniques by which geophysical parameters can be constrained are detailed. Such analysis methods include crustal thickness modeling, the analysis of geoid/topography ratios, and modeling of the spectral admittance and correlation functions. Finally, the major results that have been obtained by modeling the gravity and topography of the Earth, Venus, Mars, and the Moon are summarized.

Key words: Gravity, Topography, Geoid, Spherical Harmonics, Localized Spectral Estimation, Admittance, Coherence, Earth, Venus, Mars, Moon.

CONTENTS

1 INTRODUCTION

One of the most precise ways to investigate the subsurface structure of a planet is through the analysis of seismic waves. While such endeavors have proved to be remarkably successful for the Earth, the emplacement of a geophysical network that includes seismometers on a terrestrial body such as Mercury, Venus, Mars, or the Moon is both costly and technologically challenging (see Chapter 4). Fortunately, alternative means exist to probe the interior structure of the terrestrial planets from orbit. One such method, reviewed in Chapter 5, is through analyses of a planet's time-variable rotation. Such investigations can measure the moment of inertia factor (when combined with low-degree gravity measurements) and k_2 Love number, from which constraints on the density and viscosity profile can be obtained. The magnetic induction response of a planet to time variable magnetic fields can be used to determine how the body's electrical conductivity (and hence composition) varies with depth. Finally, because the gravitational field of a planet is sensitive to its internal density structure, another powerful method that can be used to probe the subsurface, and which is the subject of this review, is the joint analysis of gravitational and topographic data.

The past decade has witnessed dramatic advancements in our understanding and knowledge of the gravitational fields and topography of the terrestrial planets. These advances are intimately related to the acquisition of radio tracking data from orbiting spacecraft (which can be used to invert for the gravitational field), as well as the collection of data from orbiting altimeters. As examples, the first near-global topographic map of the Moon was obtained by the Clementine mission in 1994 (*Zuber et al.* 1994), and the topography of Venus and Mars was mapped to high resolution by the Magellan (*Ford and Pettengill* 1992) and Mars Global Surveyor (*Smith et al.* 1999) missions which were placed in orbit in 1990 and 1997, respectively. In addition, the topography and gravitational field of the Earth has been continually refined by a series of recent and ongoing missions.

From a geophysical perspective, the motivation for obtaining high resolution gravitational and topographic data is to place constraints on the interior structure of a planet. As a result of Newton's law of gravitation, the magnitude and direction of the gravitational acceleration exterior to a planet is completely determined by its internal distribution of mass. When combined with topographic data and reasonable geologic assumptions, it is possible to invert for important geophysical parameters such as crustal thickness, elastic thickness, and crustal and mantle density. These model parameters can then be used to address questions concerning planetary differentiation, crust formation, thermal evolution, and magmatic processes. As the spatial resolving power of gravitational measurements decreases with increasing distance from the object, such investigations are generally restricted to the crust and upper mantle.

Very few research articles have been written that review the gravitational fields and topography of the terrestrial planets from a comparative planetology perspective: exceptions include *Phillips and Lambeck* (1980), *Balmino* (1993), *Bills and Lemoine* (1995), and *Rummel* (2005). The purpose of this chapter is to both review the current state of knowledge of the gravitational fields and topography of the terrestrial planets, and to review the tools that are used to describe and analyze these data. While gravitational and topographic data sets can each be used independently to make inferences about the interior structure of a planet, such results are often based upon untestable hypotheses and/or are highly underconstrained. Thus, although regional topographic models have been constructed for some planets, moons, and asteroids (such a Mercury (e.g., *Harmon et al.* 1986; *Anderson et al.* 1996a; *Watters et al.* 2001, 2002; *André et al.* 2005), Ganymede (*Giese et al.* 1998), Europa (*Nimmo et al.* 2003b,a), Phobos (*Duxbury* 1989), and 433 Eros (*Zuber et al.* 2000b)), and the longest wavelength gravitational fields have been constrained for others (such as Mercury (*Anderson et al.* 1987), Eros (*Miller et al.* 2002; *Garmier and Barriot* 2002), Io (*Anderson et al.* 1996c, 2001a), Europa (*Anderson et al.* 1998), Ganymede (*Anderson et al.* 1996b) and Callisto (*Anderson et al.* 2001b)), this review will focus on those bodies for which the gravity and topography are both characterized to high degree; namely, the Earth, Venus, Mars, and the Moon.

The outline of this chapter is as follows. First, in section 2, a general review of the mathematical formalism that is used in describing the properties of gravitational fields topography is given. Next, in section 3, the basic properties of the gravitational fields and topography of the Earth, Venus, Mars, and the Moon are characterized. Following this, sections 4–7 discuss the relationship between gravity and topography, and how the two data sets can be used to invert for geophysical parameters. These methods include crustal thickness modeling, the analysis of geoid/topography ratios, and modeling of the spectral admittance and correlation functions. Section 8 summarizes the major results that have been obtained by gravity and topography modeling for these planetary bodies, and section 9 concludes by discussing future developments that can be expected in this domain.

2 MATHEMATICAL PRELIMINARIES

This section reviews the mathematical background that is required to understand how gravitational fields and topography are characterized and manipulated. As most analysis techniques make use of spherical harmonics, the first subsection defines these functions and introduces certain concepts such as the power spectrum. The following subsection gives definitions that are specific to the gravitational potential, gravitational field, and geoid. For further details, the reader is referred to several key books and articles such as *Jeffreys* (1976), *Kaula* (1967), *Kaula* (2000), *Heiskanen and Moritz* (1967) and *Lambeck* (1988).

2.1 Spherical harmonics

Spherical harmonics are the natural set of orthogonal basis functions on the surface of the sphere. As such, any real square-integrable function can be expressed as a linear combination of these as

$$f(\Omega) = \sum_{l=0}^{\infty} \sum_{m=-l}^{l} f_{lm} Y_{lm}(\Omega), \qquad (1)$$

where Y_{lm} is the spherical harmonic function of degree l and order m, f_{lm} is the corresponding expansion coefficient, and $\Omega = (\theta, \phi)$ represents position on the sphere in terms of colatitude θ and longitude ϕ, respectively. Alternative representations include the use of ellipsoidal harmonics (e.g., *Garmier and Barriot* 2001) when the function is globally known, and spherical cap harmonics (e.g., *Haines* 1985; *Hwang and Chen* 1997; *Thébault et al.* 2004, 2006) when the function is known only regionally. In geodesic and gravitational applications, the real spherical harmonics are defined as

$$Y_{lm}(\Omega) = \begin{cases} \bar{P}_{lm}(\cos\theta) \cos m\phi & \text{if } m \geq 0 \\ \bar{P}_{l|m|}(\cos\theta) \sin |m|\phi & \text{if } m < 0, \end{cases} \quad (2)$$

where the normalized associated Legendre functions are given by

$$\bar{P}_{lm}(\mu) = \sqrt{(2 - \delta_{0m})(2l+1)\frac{(l-m)!}{(l+m)!}} \, P_{lm}(\mu), \quad (3)$$

and where δ_{ij} is the Kronecker delta function. The unnormalized Legendre functions in the above equation are defined in relation to the Legendre Polynomials by

$$P_{lm}(\mu) = \left(1 - \mu^2\right)^{m/2} \frac{d^m}{d\mu^m} P_l(\mu), \quad (4)$$

$$P_l(\mu) = \frac{1}{2^l l!} \frac{d^l}{d\mu^l} \left(\mu^2 - 1\right)^l. \quad (5)$$

The normalized associated Legendre functions are orthogonal for a given value of m according to

$$\int\limits_{-1}^{1} \bar{P}_{lm}(\mu)\bar{P}_{l'm}(\mu) \, d\mu = 2(2 - \delta_{0m}) \, \delta_{ll'}, \quad (6)$$

and the spherical harmonics are orthogonal over both l and m with the normalization

$$\int_{\Omega} Y_{lm}(\Omega)Y_{l'm'}(\Omega) \, d\Omega = 4\pi \, \delta_{ll'}\delta_{mm'}, \quad (7)$$

where $d\Omega = \sin\theta \, d\theta \, d\phi$. Multiplying eq. 1 by $Y_{l'm'}$ and integrating over all space, the spherical harmonic coefficients of the function f can be obtained by calculating the integral

$$f_{lm} = \frac{1}{4\pi} \int_{\Omega} f(\Omega)Y_{lm}(\Omega) \, d\Omega. \quad (8)$$

A useful visualization property of the spherical harmonic functions is that they possess $2|m|$ zero crossings in the longitudinal direction, and $l - |m|$ zero crossings in the latitudinal direction. In addition, for a given spherical harmonic degree l, the equivalent Cartesian wavelength is $\lambda \approx 2\pi R/\sqrt{l(l+1)}$, where R is the mean planetary radius, a result known as the Jeans relation. It should be noted that those coefficients and spherical harmonics where $m = 0$ are referred to as zonal, those with $l = |m|$ are sectoral, and the rest are tesseral. Furthermore, the zonal coefficients C_{l0} are often written as $-J_l$.

Using the orthogonality properties of the spherical harmonic functions, it is straightforward to verify that the total power of a function f is related to its spectral coefficients by a generalization of Parseval's theorem:

$$\frac{1}{4\pi} \int_{\Omega} f^2(\Omega) \, d\Omega = \sum_{l=0}^{\infty} S_{ff}(l), \quad (9)$$

where

$$S_{ff}(l) = \sum_{m=-l}^{l} f_{lm}^2 \quad (10)$$

is referred to as the power spectrum of the function. (The term "power" is here used in the sense of the signal processing literature; namely, the square of the function divided by the area that it spans.) It can be shown that S_{ff} is unmodified by a rotation of the coordinate system. Similarly, the cross-power of two functions f and g is given by

$$\frac{1}{4\pi} \int_{\Omega} f(\Omega)g(\Omega) \, d\Omega = \sum_{l=0}^{\infty} S_{fg}(l), \quad (11)$$

where

$$S_{fg}(l) = \sum_{m=-l}^{l} f_{lm} \, g_{lm} \quad (12)$$

is defined as the cross-power spectrum. If the functions f and g have a zero mean (i.e., their degree-0 terms are equal to zero), then $S_{ff}(l)$ and $S_{fg}(l)$ represent the contributions to the variance and covariance, respectively, for degree l. Some authors plot routinely the power per degree, $S/(2l+1)$, or the rms amplitude of the spherical harmonic coefficients, $\sqrt{S/(2l+1)}$.

One source of confusion with spherical harmonic analyses is that not all authors use the same definitions for the spherical harmonic and Legendre functions. In contrast to the "geodesy" or "4π" normalization of eq. 7 (cf. *Kaula* 2000), the seismology (e.g., *Dahlen and Tromp* 1998) and physics (e.g., *Varshalovich et al.* 1988) communities often use orthonormal harmonics, whose squared integral is equal to unity. Alternatively, the geomagnetic community employs Schmidt semi-normalized harmonics whose squared integral is $4\pi/(2l+1)$ (e.g., *Blakely* 1995). A more subtle problem is related to a phase factor of $(-1)^m$ (the Condon-Shortley phase) that is sometimes applied to either eqs 3 or 4. While the spherical harmonics used by the geodesy and geomagnetic communities both exclude this phase factor, those in the physics and seismology communities often include it.

In order to obtain the spherical harmonic coefficients f_{lm} of a function f, it is necessary to be able to calculate accurately both the normalized Legendre functions of eq. 3 and the integral of eq. 8. Methods for efficient calculation of the normalized associated Legendre functions depend upon the use of well known three-term recursion formulas. If starting values used in the recursion are appropriately scaled, as is summarized by *Holmes and Featherstone* (2002), these can be computed to high accuracy up to a maximum spherical harmonic degree of about 2700. To obtain a similar accuracy at higher degrees would require the use of an alternative scaling algorithm.

The integrals of eq. 8 are most easily performed if the function f is known on a set of evenly spaced grid points in longitude. Numerical methods for calculating this integral generally involve Fourier transforming each latitudinal band, and then integrating over latitude for each l and m

(e.g., *Sneeuw* 1994). If the function is sampled on an $n \times n$ grid, with n even, and if the function is known to be band-limited to a maximum degree $n/2 - 1$, then the spherical harmonic transform can be computed exactly (see *Driscoll and Healy* 1994). Alternatively, the integral over latitude can be performed using Gauss-Legendre quadrature (e.g., *Press et al.* 1992, pp. 140–149). While the integrand of eq. 8 is not in general a terminating polynomial, if the function is band-limited to a maximum degree n, $n + 1$ points in latitude are sufficient to calculate accurately the spherical harmonic expansion coefficients. Software for performing spherical harmonic transforms and reconstructions is available at the author's website (see Table 1 for a list of internet resources).

2.2   The potential, gravity, and geoid

If the gravitational acceleration **g** is expressed as the gradient of a scalar potential U,

$$\mathbf{g}(\mathbf{r}) = \nabla U(\mathbf{r}), \tag{13}$$

Newton's law can be used to calculate the gravitational potential at an arbitrary point by a simple integral over the mass distribution,

$$U(\mathbf{r}) = \int_V \frac{G\,\rho(\mathbf{r}')}{|\mathbf{r} - \mathbf{r}'|}\,dV', \tag{14}$$

where **r** represents position, ρ is the mass density and V signifies that space which is occupied by the body. While the sign convention of the above two equations is consistent with that used in the geodesy literature, it should be noted that other disciplines, such as physics, place a negative sign in front of each of these. Exterior to the mass distribution V, it can be shown that the potential satisfies Laplace's equation (e.g., *Kaula* 2000, Chap. 1):

$$\nabla^2 U(\mathbf{r}) = 0. \tag{15}$$

By use of the above identity and the method of separation of variables, the potential U exterior to V can be expressed alternatively as a sum of spherical harmonic functions:

$$U(\mathbf{r}) = \frac{GM}{r} \sum_{l=0}^{\infty} \sum_{m=0}^{l} \left(\frac{R_0}{r}\right)^l C_{lm}\, Y_{lm}(\Omega). \tag{16}$$

Here, the C_{lm}s represent the spherical harmonic coefficients of the gravitational potential at a reference radius R_0, G is the gravitational constant, and M is the total mass of the object. In practice, the infinite sum is truncated beyond a maximum degree L that is justified by the data resolution. The coefficients C_{lm} of eq. 16 are uniquely related to the internal mass distribution of the body, and methods for calculating these are deferred until section 4. Here, it is only noted that the degree-0 coefficient C_{00} is equal to unity, and that if the coordinate system has been chosen such that it coincides with the center of mass of the object, the degree-1 terms (C_{10}, C_{11} and C_{1-1}) are identically zero.

As a result of the factor $(R_0/r)^l$ that multiplies each term in eq. 16, the high frequency components in this sum (i.e., those with large l) will be attenuated when the observation radius r is greater than the reference radius R_0. In contrast, if the coefficients were determined at the altitude of an orbiting satellite, and if this equation were used to determine the potential field at the surface of the planet, then the high frequency terms would instead be relatively amplified. Since the spherical harmonic coefficients always possess some uncertainty, which generally increases with increasing l, the process of downward continuing a potential field is not stable and must generally be compensated by some form of filtering (e.g., *Phipps Morgan and Blackman* 1993; *Wieczorek and Phillips* 1998; *Fedi and Florio* 2002).

If the body under consideration is rotating, then an additional non-gravitational force must be taken into account when calculating the potential. In the reference frame of the rotating body, this can be accounted for by adding to eq. 16 a pseudo-potential term that is a result of the centrifugal force. This rotational potential, as well as its spherical harmonic expansion, is given by

$$U^{rot} = \frac{\omega^2 r^2 \sin^2\theta}{2} = \omega^2 r^2 \left(\frac{1}{3}Y_{00} - \frac{1}{3\sqrt{5}}Y_{20}\right), \tag{17}$$

where ω is the angular velocity of the rotating object. For some applications, especially concerning the Earth and Moon, it is necessary to include the tidal potential of the satellite or parent body when calculating the potential (see *Zharkov et al.* 1985; *Dermott* 1979). For a synchronously locked satellite on a circular orbit, such as the Moon, the combined tidal and rotational potential in the rotating frame is (ignoring degree-0 terms that do not depend upon r) given approximately by

$$U^{tide+rot} \approx \omega^2 r^2 \left(\frac{1}{3}Y_{00} - \frac{5}{6\sqrt{5}}Y_{20} + \frac{1}{4}\sqrt{\frac{12}{5}}Y_{22}\right). \tag{18}$$

An important quantity in both geodesy and geophysics is the geoid, which is defined to be a surface that possesses a specific value of the potential. (Although one could come up with imaginative names for equipotential surfaces on Venus, Eros, and Io, among others, the term *geo*id will here be used for all.) As there are no tangential forces on an equipotential surface (see eq. 13), a static fluid would naturally conform to the geoid. The oceans of the Earth are approximately static and are well approximated by such a surface. In geophysics, stresses within the lithosphere are often calculated by referencing the vertical position of a density contrast to an equipotential surface. This is necessary when performing lithospheric flexure calculations, especially when considering the longest wavelengths.

The height N of an equipotential surface above a spherical reference radius R can be obtained by approximating the potential by a Taylor series

$$U(R + N) \approx U(R) + \frac{dU(R)}{dr}N + \frac{1}{2}\frac{d^2U(R)}{d^2r}N^2, \tag{19}$$

and setting this expression equal to a constant

$$U(R + N) = \frac{GM}{R} + \frac{\omega^2 R^2}{3}, \tag{20}$$

the value of which is here chosen to be the degree-0 term of the potential at the reference radius R for a rotating planet. Since this equation is quadratic in N, the geoid height can be solved for analytically at any given position. Analytic expressions for the partial derivatives of the potential are easily obtained in the spectral domain from eqs 16 (see 22) and 17, and spatial renditions of these can be obtained by performing the inverse spherical harmonic transform.

Table 1. Internet resources.

Resource	Internet address
SHTOOLS: Fortran 95 spherical harmonics code	http://www.ipgp.jussieu.fr/~wieczor/
Planetary Data System (PDS) Geosciences node	http://pds-geosciences.wustl.edu/
ETOPO2: Earth topography model	http://www.ngdc.noaa.gov/mgg/fliers/01mgg04.html
GTOPO30: Earth topography model	http://edcdaac.usgs.gov/gtopo30/gtopo30.asp
SRTM: Earth topography model	http://srtm.usgs.gov/ and
	ftp://e0srp01u.ecs.nasa.gov
STRM30_PLUS: Earth topography model	http://topex.ucsd.edu/WWW_html/srtm30_plus.html
WGS84 ellipsoid and "WGS84 EGM96 geoid"	http://earth-info.nga.mil/GandG/wgs84/
GGM02: Earth gravity model	http://www.csr.utexas.edu/grace/gravity/
EIGEN: Earth gravity models	http://www.gfz-potsdam.de/pb1/op/grace/results/
GTDR3.2: Venus topography	ftp://voir.mit.edu/pub/mg_3003/
Planetary maps with feature names	http://ralphaeschliman.com/
Generic Mapping Tools	http://gmt.soest.hawaii.edu/

For most cases it is sufficient to use only the first order terms of eq. 19. Specifically, if the first derivative of U is approximated by $-GM/R^2$, then the geoid is simply given by

$$N \approx R \sum_{l=2}^{\infty} \sum_{m=-l}^{l} \left(\frac{R_0}{R}\right)^l C_{lm} Y_{lm} - \frac{\omega^2 R^4}{3\sqrt{5}GM} Y_{20}, \quad (21)$$

where the degree-1 terms have been assumed to be zero. Although the maximum difference between the first and second order methods is less than 3 meters for both the Moon and Venus, differences of up to 20 and 40 meters are obtained for the Earth and Mars, respectively. The poor performance of the first-order approximation for the Earth and Mars is primarily a result of the large rotationally induced J_2 potential terms.

Despite the simplicity of the above method for obtaining the height to an equipotential surface, the question arises as to *which* equipotential surface should be used. For the Earth, a natural choice is the potential corresponding to mean sea level. However, for the other planets, the choice is more arbitrary. As the above equations for calculating the potential are strictly valid only when the observation point is exterior to the body, one manner of picking a specific potential might be to chose that value for which all points on the geoid are exterior to the body. (Calculation of the potential below the surface of a planet would require knowledge of the interior density distribution.) Another standard definition might be to use the mean potential on the planet's equator.

The radial component of the gravitational field is easily calculated by taking the first radial derivative of eq. 16. Ignoring the rotational potential, and using the sign convention that gravitational accelerations are positive when directed downward, this is given by the expression

$$g_r = \frac{GM}{r^2} \sum_{l=0}^{\infty} \sum_{m=-l}^{l} \left(\frac{R_0}{r}\right)^l (l+1) C_{lm} Y_{lm}. \quad (22)$$

Note that this equation differs from that of the potential only by the inclusion of the additional factors $1/r$ and $(l+1)$. The second factor gives a greater importance to the higher degree terms, and it is for this reason that plots of the potential and geoid appear to be "smooth" when compared to components of the gravitational field. In terrestrial applications it is common to calculate the gravitational field on the geoid.

By inserting eq. 21 into eq. 22, and ignoring rotational and higher-order terms, it can be shown that the radial component of the gravitational field on the geoid can be calculated simply by replacing the term $(l+1)$ in eq. 22 by $(l-1)$. The standard unit for quantifying gravitational perturbations is the Galileo, where $1\,\text{Gal} = 10^{-2}\,\text{m s}^{-2}$, and when plotting gravitational anomalies in map form, it is conventional to use mGals.

Finally, it will be useful to characterize the relationship between the gravitational field and topography in the spectral domain. For this, let us presume that the radial gravity g_{lm} and topography h_{lm} are related by

$$g_{lm} = Q_{lm} h_{lm} + I_{lm}, \quad (23)$$

where Q_{lm} is a linear non-isotropic transfer function, and I_{lm} is that portion of the gravitational signal, such as noise, that is not predicted by the model (the topography can generally be considered noise free). If I_{lm} is uncorrelated with the topography, then it is straightforward to show that the expectations of both S_{hh} and S_{hg} will be unaffected by this signal. (This can be shown by multiplying eq. 23 by h_{lm}, summing over all m, and taking the expectation.) In contrast, the expectation of the gravitational power spectrum will depend upon the magnitude of I_{lm}. In particular, for the case where I_{lm} is a random variable that is independent of the surface topography, the expectation of the gravitational power spectrum is simply

$$S_{gg}(l) = S_{gg}^0(l) + S_{II}(l), \quad (24)$$

where S_{gg}^0 is the power spectrum predicted exclusively by the model Q_{lm}, and S_{II} is the power spectrum of I_{lm}. Thus, gravitational measurement noise will bias the gravitational power spectrum by an additive constant.

In quantifying the relationship between gravity and topography it is useful to work with ratios of their cross-power spectra. One quantity, referred to as the *admittance* is defined by the cross-power of the two functions divided by the power of the topography (e.g., *Dorman and Lewis* 1970):

$$Z(l) = \frac{S_{hg}(l)}{S_{hh}(l)}. \quad (25)$$

This function is not biassed by the presence of noise, and when the transfer function Q_{lm} is isotropic (i.e., independent of m), it is an unbiassed estimate of Q_l. Another ratio that is commonly used, which is dimensionless, is

$$\gamma(l) = \frac{S_{hg}(l)}{\sqrt{S_{hh}(l)S_{gg}(l)}}. \qquad (26)$$

If for a given degree l the coefficients h_{lm} and g_{lm} possess a zero mean, the above function is simply the degree-correlation of the two sets of harmonic coefficients, which can possess extreme values of 1 and -1. While noise will not bias the admittance function, it will bias the degree-correlation function towards lower values as a consequence of the gravitational power spectrum in the denominator of this expression. The term *coherence* is usually reserved for the correlation squared, but this definition is not universally followed. Since squaring the correlation discards its sign, its use is not advocated here. It is noted that the isotropic version of eq. 23 predicts that the spectral correlation coefficient should always be ± 1. Nevertheless, as discussed in section 7, non-isotropic models yield expressions that are wavelength-dependent. While other ratios of cross-power spectra could be constructed, only two will be independent.

3 THE DATA

3.1 The Earth

3.1.1 Topography

Despite the fact that the measurement of the Earth's topography and bathymetry has been the subject of numerous government supported campaigns, large portions of the Earth's surface, namely the oceans, remain poorly characterized. Indeed, from a global perspective, it can be said that the topography of Venus and Mars is better known than that of the planet we call home. Until recently, even the elevations of the aerial portions of the continents possessed long-wavelength uncertainties, a result of mosaicking numerous elevation models, each with its own reference surface, along artificial political boundaries. While major advances have been made in the past decade towards generating global models, the main deficiency is still the sparse bathymetry of the oceans.

Numerous topographic models of the Earth's landmass have been assembled from various sources over the past few decades, including ETOPO5 and ETOPO2 (5- and 2-arcminute resolution, *National Geophysical Data Center* 2001), GLOBE (30 arcsecond resolution, see *Hastings and Dunbar* 1999) and GTOPO30 (detailed documentation for these and all following topography models can be found at the appropriate web address listed in Table 1). Currently, the most accurate model of the Earth's landmass comes from radar interferometric data collected by the Shuttle Radar Topography Mission (SRTM). During its ten days of operation onboard the US space shuttle in year 2000, this mission mapped nearly 80 percent of the landmass between 60° N and 54° S with a horizontal sampling of 1 arcsecond ($\sim$30 meters) and an absolute vertical accuracy better than about 10 meters (*Rabus et al.* 2003; *Rodríguez et al.* 2005). Because of the 5.6 cm wavelength of the radar, elevations generally correspond to the top of the canopy when vegetation is present.

The bathymetry of the oceans has been measured from ship surveys using echo sounding for over half a century. Unfortunately, the ship tracks sometimes possess large nav-

igational errors, and large data gaps exist. As reviewed by *Marks and Smith* (2006), many datasets exist that are based upon these measurements, but each has its own peculiarities. In the absence of additional ship survey data, one method that can be used to improve the bathymetry of the oceans is by combing ship survey data with marine gravity data. As is detailed by *Smith and Sandwell* (1994, 1997), marine gravity anomalies (as obtained from altimeter derived sea surface slopes) are highly correlated with seafloor topography over a restricted wavelength band. By combining predicted topography from bandpassed gravity anomalies with the long wavelength bathymetry from shipboard sounding, it has been possible to obtain near-global 2-arcsecond resolution estimates of seafloor topography. Nevertheless, it should be emphasized that such data products are indeed estimates, and that they may be inappropriate for certain types of geophysical modeling.

Global Earth topography models that combine oceanic bathymetry and landmass topography include ETOPO2 and SRTM30_PLUS. The later of these represents a combination of the SRTM 30-arcsecond data and the *Smith and Sandwell* (1997) predicted bathymetry, with gaps filled by GTOPO30 data, among others. An image of this global topographic model is displayed in Figure 1. This dataset represents elevations above the "WGS84 EGM96 geoid", which is a good approximation of "mean sea level" (see internet documentation in Table 1 for precise definitions). If absolute radii of the Earth were desired (as is necessary for most methods that calculate gravity from topography), it would be necessary to add this geoid, which is referenced to the WGS84 ellipsoid, and the WGS84 ellipsoid itself. The WGS84 ellipsoid is a good representation of the Earth's zonal shape, and possesses a 21 km rotationally induced difference in elevation between the equator and polar axis.

3.1.2 Gravity

The gravitational field of the Earth has been mapped by several techniques, including analyses of satellite tracking data, terrestrial measurement campaigns, and satellite altimetry of the ocean surface (geoid slopes are proportional to the gravity field in the spectral domain (see, among others *Hwang and Parsons* 1996; *Sandwell and Smith* 1997)). The construction of global high-resolution models generally consists of combing the long-wavelength information from satellite tracking data with the short wavelength information in the terrestrial and oceanic altimeter surveys. The model EGM96 (*Lemoine et al.* 1998) has been the standard reference for much of the past decade, but this has been superseded by data obtained from the recent missions CHAMP and GRACE.

In contrast to the EGM96 model that is based upon satellite tracking data from terrestrial stations, the ongoing missions CHAMP (*Reigber et al.* 2004) and GRACE (*Tapley et al.* 2004) are based upon continuous satellite to GPS (global positioning system) tracking data. While CHAMP is a single satellite, GRACE consists of two satellites on identical orbits of which the distance between the two is measured to high accuracy by a microwave communication link. Two of the most recent high resolution models of the Earth's gravitational field derived from these data include GGM02C (*Tapley et al.* 2005) and EIGEN-GL04C (cf. *Reigber et al.*
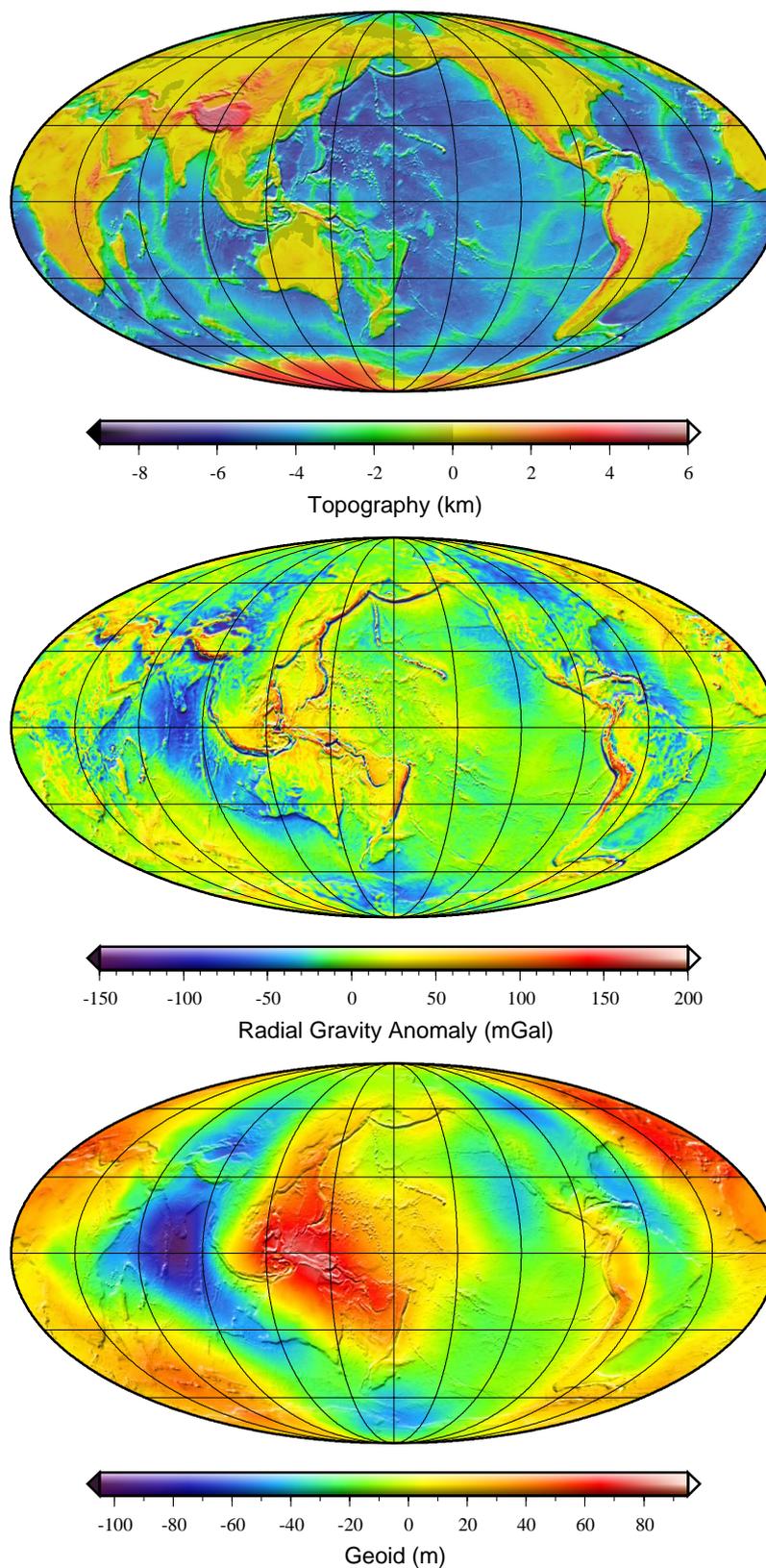
Figure 1. (top) Global topography and bathymetry of the Earth, referenced to mean sea level, of the model SRTM30_PLUS. (middle) Radial free-air gravity from EIGEN-GL04C, obtained after setting the zonal degree-2 term equal to zero, evaluated at a radius of 6378.1 km. (bottom) First-order approximation to the geoid obtained from the same coefficients as the radial gravity field. All images are in a Mollweide projection with a central meridian of 180° W longitude and are overlain by a gradient image derived from the topographic model.

2005). GGM02C is based upon GRACE tracking data combined with terrestrial and altimeter based surface measurements and is valid to degree 200 (this can be augmented to degree 360 by using the EGM96 spherical harmonic coefficients). In contrast, EIGEN-GL04C is valid to degree 360 ($\lambda \approx 110$ km) and additionally makes use of laser ranges to the LAGEOS satellites.

Images of the radial gravitational anomaly and geoid, as determined from eqs 21 and 22, respectively, are shown in Figure 1 for the model EIGEN-GL04C. For both images, the zonal degree-2 term that is primarily a result of the rotational flattening was set to zero, and the fields were evaluated at a reference radius of 6378.1 km. (The shape and potential of a flattened ellipsoid are well approximated by the degree-2 zonal harmonic.) The largest gravitational anomalies are seen to be correlated with topography (such as trenches and seamounts), and the geoid height is found to vary by about 200 meters. Errors in the geoid and gravity field are estimated to be approximately 30 cm and 8 mGal, respectively.

3.1.3 *Spectral analysis*

A spherical harmonic model of the Earth's shape was constructed by adding the EGM96 and WGS84 geoid and ellipsoid, respectively, to the model SRTM30_PLUS, and expanding this gridded data set to degree 719 using the method of *Driscoll and Healy* (1994). For the analyses presented here, the radius of the ocean floor was increased by 1030/2670 times its depth in order to convert the mass of the overlying sea water into "rock equivalent topography" (this model is here designated as SRTMP719 RET). Spectral and cross-spectral properties of this model and the EIGEN-GL04C potential are plotted in Figure 2. As demonstrated in the left panel, the power spectrum of the geoid is about 5 orders of magnitude less than that of the topography, which is a reflection of the low amplitudes of the geoid undulations present in Figure 1. The (calibrated) error spectrum of the potential model demonstrates that the coefficients are well determined at low degrees, with uncertainties gradually increasing to a near constant value close to degree 100. As a result of the $\sim$400 to 500-km altitude of the GRACE and CHAMP satellites, the contribution to the gravitational field from the orbital tracking data is necessarily limited to degrees less than about 100; the higher-degree terms are constrained almost entirely by the surface measurements.

The admittance and correlation spectra between the radial gravity and topography are plotted in the right panel of Figure 2. The correlation for many of the lowest degrees is seen to be small, and in some cases negative. Beyond degree 12 the correlation is relatively constant with a value of $\sim$0.6–0.7, though it should be noted that this function slightly decreases with increasing degree beyond degree $\sim$250. If the surface topography were completely uncompensated, which should be a good approximation beyond degree 200, then the admittance would have a near-constant value of $2\pi\rho G$, or 42 mGal km^{-1} times the surface density in units of g cm^{-3}. The observed function is everywhere lower than this theoretical value by a factor of two, and this is a consequence of the fact that the gravity and topography are not perfected correlated on a global scale (see discussion in Section 6.2).

3.2 Venus

3.2.1 *Topography*

The planet Venus possesses a dense atmosphere and is perpetually enshrouded by opaque clouds of sulphuric acid. In order to obtain measurements of the surface, it is necessary to make use of electromagnetic frequencies, such as microwaves, where the atmosphere is transparent. Surface elevations of Venus have been measured from orbit using radar altimeters onboard the missions Pioneer Venus Orbiter, Venera 15 and 16, and Magellan. Of these, the Magellan spacecraft, which was in orbit between 1990 and 1994, collected the highest resolution measurements on a near-global scale (for a detailed description, see *Ford and Pettengill* 1992).

As a result of the elliptical orbit of the Magellan spacecraft, the spatial resolution of the elevation measurements varied between 8×10 km at periapse to 19×30 km at the north pole (*Rappaport et al.* 1999). Over 4 million range measurements were ultimately collected, and these were used to construct a 5×5 km gridded elevation model. With the exception of a few relatively minor data gaps covering about 2.6% of the planet's surface area, coverage of the planet is fairly uniform. (If data from previous missions are used to fill the gaps, then just less than 1% of the planet is not covered at this resolution). Though the spacecraft-surface range measurements are estimated to have an accuracy of less than 10 meters (errors can be larger over rough and steeply sloping terrain), uncertainties in the spacecraft orbit at the time of initial processing were sometimes much greater, especially during superior conjunction. The most recent gravity model of *Konopliv et al.* (1999) has considerably improved the spacecraft navigational errors, and these improved orbit predictions have been used by *Rappaport et al.* (1999) in a complete reprocessing of the altimetry data set (archived as GTDR3.2). Horizontal uncertainties in the footprint locations are insignificant in comparison to the footprint size, and the RMS radial uncertainty is estimated to be less than 20 meters.

An image of the Venusian topography (derived from the spherical harmonic model VenusTopo719; see below) is shown in Figure 3, where it is referenced to the geoid. While the hypsometry of Venus is unimodal (e.g., *Ford and Pettengill* 1992; *Rosenblatt et al.* 1994), in contrast to that of the Earth which is bimodal, Venus can be broadly characterized by its low-lying plains, "continental" plateaus, and volcanic swells. The most prominent highlands include Aphrodite Terra, which lies along the equator, and Ishtar Terra, which is located at high northern latitudes. Ishtar and Aprhodite Terra differ in that the former is flanked by high elevation mountain ranges. Isolated domical volcanic provinces that possess prominent rift valleys include Atla (0° N, 200° E) and Beta (25° N, 280° E) Regiones. The highest topographic excursion corresponds to Maxwell Montes, located in Ishtar Terra, which reaches more than 10 km above the surrounding plains. (Maps with feature names for Venus, Mars, and the Moon can be found at the appropriate web address in Table 1).

3.2.2 *Gravity*

Models of the gravitational field of Venus have been constructed through the analyses of tracking data from the Pio-
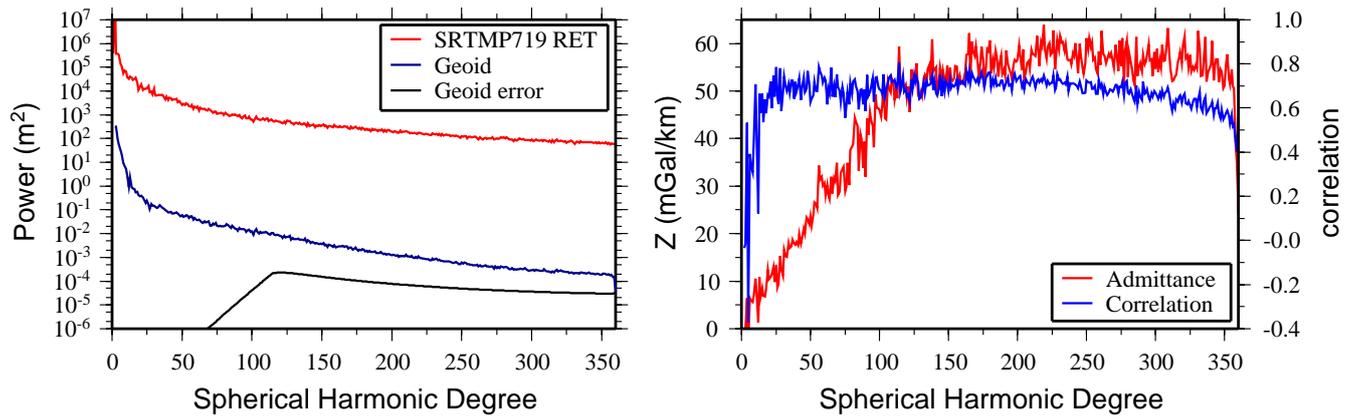
Figure 2. Power and cross-power spectra of the Earth's radial gravity and topography. (left) Power spectra of the topography (SRTMP719 RET), geoid (EIGEN-GL04C), and calibrated geoid error. (right) Admittance and correlation spectra of the radial gravity and topography.

neer Venus Orbiter and Magellan spacecraft (for a review, see *Sjogren et al.* 1997). The orbit of the Pioneer Venus spacecraft was highly eccentric, and possessed periapse altitudes as low as 150 km near the equator. The Magellan spacecraft was initially on an eccentric orbit as well, but through the technique of aerobraking during the gravity mapping phase of the mission, the orbit was transformed to a more circular one, with periapse and apoapse altitudes varying between 155–220 and 350–600 km, respectively.

The most recent model of the Venusian gravitational field is the degree 180 JPL (Jet Propulsion Laboratory) model MGNP180U of *Konopliv et al.* (1999). Because of computational constraints at the time, this model was constructed in three phases. In the first step, a model to degree 120 was generated using the full unconstrained covariance matrix and a spatial *a priori* constraint that depended on the strength of the gravitational accelerations (such models are labeled SAAP for Surface Acceleration *A Priori*). The second step used this model as the nominal solution, and then solved for the coefficients from degree 116 to 155 using the same spatial constraint. For the third step, the coefficients were determined from degree 154 to 180, but instead of using a spatial constraint, the spherical harmonic coefficients were biased towards a global power law (i.e., a "Kaula rule"). Future models could be improved by performing the inversion in a single step. As a result of the spatial constraint that was employed in the first two steps, the spatial resolution of the model varies dramatically with position on the surface. While spectral resolutions approaching degree 180 may be realized close to the equator, other regions possess resolutions as low as degree 40 (see figure 3 of *Konopliv et al.* 1999).

Images of the MGNP180U radial gravitational field and geoid are presented in Figure 3, evaluated at a radius if 6051 km, where the spectral coefficients have been truncated beyond degree 65. As a result of the slow retrograde rotation of Venus, there is no appreciable rotational flattening of the planet, and the J_2 potential coefficient is thus here included in contrast to that of the Earth and Mars. These plots show that most gravitational and geoid anomalies are highly correlated with the surface topography. The largest radial gravitational anomalies are associated with the volcanoes Maat and Ossa Mons in Atla Regio, with values reaching about

270 mGal. The high elevations of Maxwell Montes, Beta Regio, and numerous smaller volcanic provinces, are also seen to possess significant anomalies. Uncertainties in the radial component of the gravitational field are typically 10 mGal at the surface, but can be as high as 50 mGal in places.

Like the Earth, the geoid undulations of Venus possess a dynamic range of only ∼200 meters. The largest geoid anomalies correspond to the volcanic swells of Atla and Beta Regiones, and the continental regions of Aphrodite and Ishtar Terra. It is also seen that the plains with the lowest elevations possess negative geoid anomalies. Uncertainties in the geoid are typically 1 meter, but can reach values as high as 4 m.

3.2.3 Spectral Analysis

A degree 719 spherical harmonic model (VenusTopo719) was constructed based on the Magellan GTDR3.2 sinusoidally projected data product. Missing nodes were filled by data obtained by the Pioneer Venus and Venera 15/16 missions, the remaining gaps were filled by interpolation using the GMT (*Wessel and Smith* 1991) command "surface" with a tension parameter of 0.35, and the spherical harmonic expansion was performed using the sampling theorem of *Driscoll and Healy* (1994). While the resulting power spectrum was found to be insensitive to changes in the tension parameter, the mean planetary radius varied by about one meter among the various models. A comparison between this spherical harmonic model and the one of *Rappaport et al.* (1999) shows that the latter suffers from an increasing loss of fidelity with increasing degree (the degree correlation between the two models is ∼ 0.93 at degree 360). While the cause for this is uncertain, possible explanations might be the use of inaccurate Legendre functions or the presence of short-wavelength aliases at high degrees.

Power spectra of the Venusian topography (VenusTopo719) and geoid (MGNP180U) are shown in the left panel of Figure 4. These are similar to those of the Earth, with the exception that the amplitudes of the degree-1 and -2 topographic terms for Venus are relatively smaller. On a log-log plot (not shown), a change in slope of the topographic power spectrum is seen to occur near degree 100 (*Rappaport et al.* 1999). While this feature might be
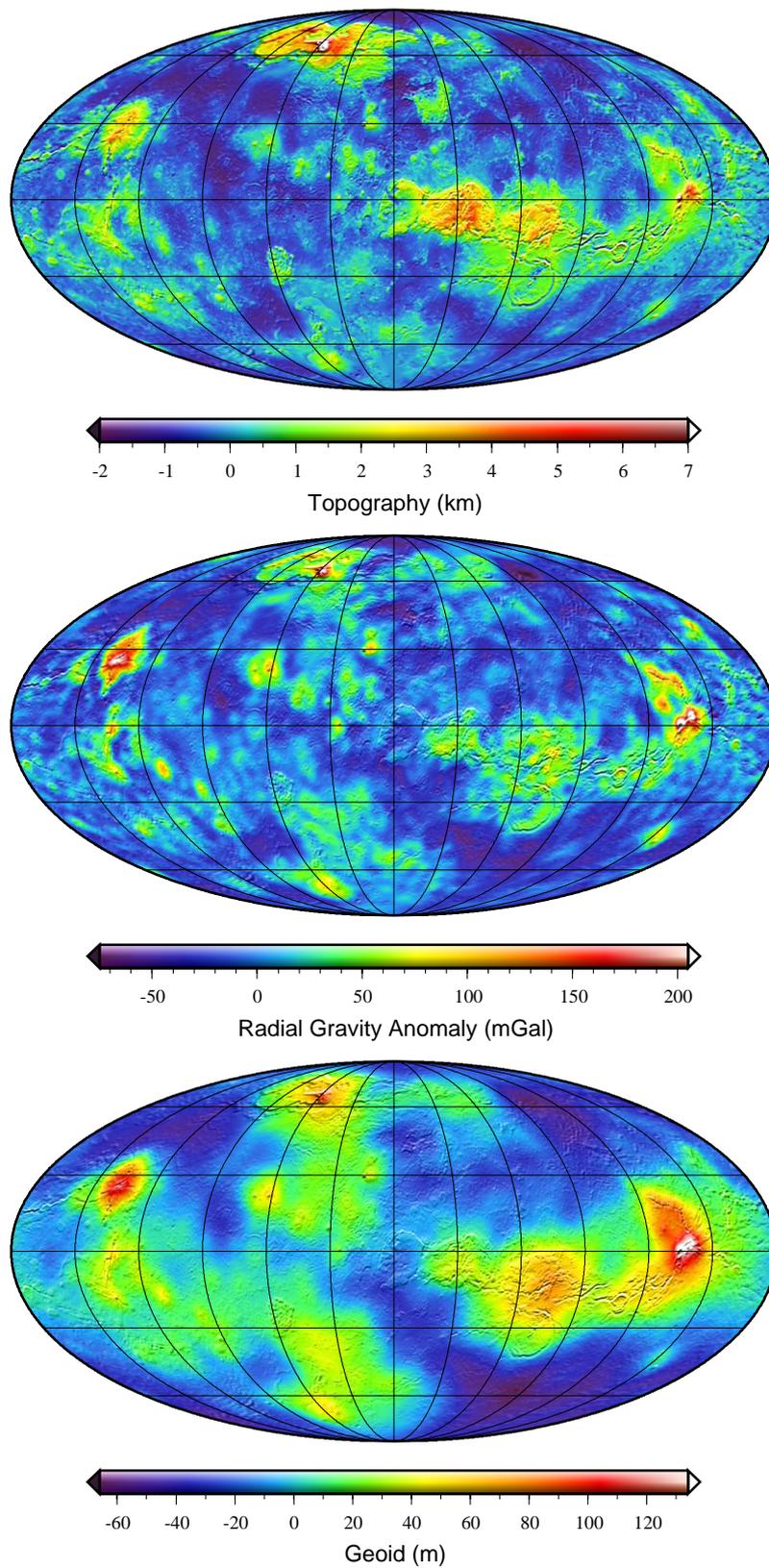
Figure 3. (top) Global topography of Venus, derived from the spherical harmonic model VenusTopo719, referenced to geoid. (middle) Radial free-air gravity, evaluated at a radius of 6051 km, obtained after truncating the spherical harmonic coefficients of MGNP180U beyond degree 65. (bottom) First-order approximation to the geoid obtained from the same coefficients as the radial gravity field. All images are in a Mollweide projection with a central meridian of 60° E longitude and are overlain by a gradient image derived from the topographic model.
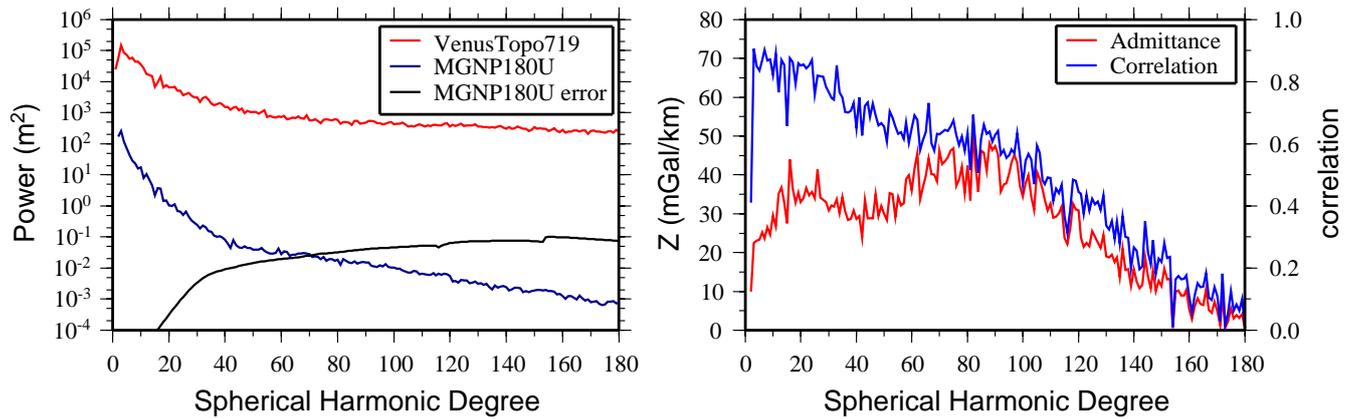
Figure 4. Power and cross-power spectra of the gravity and topography of Venus. (left) Power spectra of the topography (VenusTopo719), geoid (MGNP180U), and geoid error. (right) Admittance and correlation spectra of the radial gravity and topography.

real, it is also possible that it is related to interpolating over data gaps before performing the spherical harmonic expansion. The error spectrum of the geoid is seen to be greater than the geoid itself for degrees greater than 65. While the global values of the potential coefficients are generally unreliable beyond this degree, it should be noted that the spatial resolution of the gravitational field is a strong function of position on the surface. Discontinuities in the error spectrum are artifacts of solving for the potential coefficients in three separate steps.

The spectral admittance and correlation functions for the radial component of the gravitational field and topography, plotted in the right panel of Figure 4, are seen to differ significantly from those for the Earth. The admittance is found to possess values between ∼30 and 50 mGal/km for degrees up to degree 100, whereas for the Earth, the admittance linearly increases from ∼0 to 30 mGal/km at degree 100. The correlation between the gravitational field and topography is also significantly higher for degrees less than 40 than it is for the Earth. Nevertheless, beyond degree 60, the spectral correlation and admittance are seen to linearly decrease with increasing degree, which is a result of the poor determination of the global potential coefficients. It is of note that both the admittance and correlation for degree 2 are significantly smaller than the neighboring values. As these are unaffected by the slow retrograde rotation of Venus, these low values may demand an origin that is distinct from the higher degrees.

Because the Pioneer Venus Orbiter and Magellan spacecraft were in near polar orbits, the gravity field is better determined for the near-sectoral terms. Sectoral terms correspond to when $|m| = l$, for which the corresponding spherical harmonic functions do not possess any latitudinal zero crossings. By considering only those coefficients where $l - |m| < 20$, *Konopliv et al.* (1999) have shown that both the admittance and correlation between gravity and topography are considerably greater than when considering all coefficients combined. In particular, the correlation function remains close to 0.7 for degrees up to 140, at which point it decreases substantially. Thus, while high-degree localized spectral analyses may be justified on Venus, the fidelity of the spectral estimates will be a strong function of both position and the spherical-harmonic degree and order.

3.3 Mars

3.3.1 Topography

Prior to the 1990s, the best Martian topographic models were constructed by a combination of Earth-based radar data, spacecraft radio occultations, and stereo and photoclinometric observations, all of which suffered from either large uncertainties or a limited spatial extent (for a review, see *Esposito et al.* 1992). The laser altimeter onboard the Mars Global Surveyor spacecraft (MOLA; Mars Orbiting Laser Altimeter) has since collected an impressive data set that has revolutionized studies of the Martian surface (see *Smith et al.* 1999; *Zuber et al.* 2000a; *Smith et al.* 2001b).

After being inserted into orbit in 1997, MOLA made more than 640 million ranges to the surface over the period of four years. The spot size of the laser at the surface was ∼168 m, and these were spaced every 300 meters in the along-track direction of the spacecraft orbit. The intrinsic range resolution of the instrument was 37.5 cm, but range precision decreases with increasing surface slope, and could be as poor as 10 meters for slopes near 30°. While the along-track orbit errors are less than the size of the laser footprint, radial orbit errors could sometimes be as high as 10 meters. Nevertheless, these orbit-induced errors could be minimized by the use of altimetric crossovers. Crossovers occur whenever two altimeter ground tracks intersect, and the difference in the two elevation measurements is largely a reflection of errors in the orbit determination. By parameterizing these uncertainties by a slowly varying function, the crossover residuals can be minimized (*Neumann et al.* 2001). Such a procedure was capable of reducing the rms crossover residuals from about 8.3 to 1.8 m. Using these methods, it has been possible to measure temporal variations in CO_2 snow depth that can reach 2 meters in the polar regions (*Smith et al.* 2001a).

The topography of Mars (as determined from the 719-degree spherical harmonic model MarsTopo719; see below) referenced to the geoid (calculated to second-order accuracy) is displayed in Figure 5. Two of the most remarkable features are the dichotomy in elevation between the northern and southern hemispheres, and the regionally high elevations of the Tharsis volcanic province which is centered near the equator at 100° W. These two features give rise to a 3.3 km
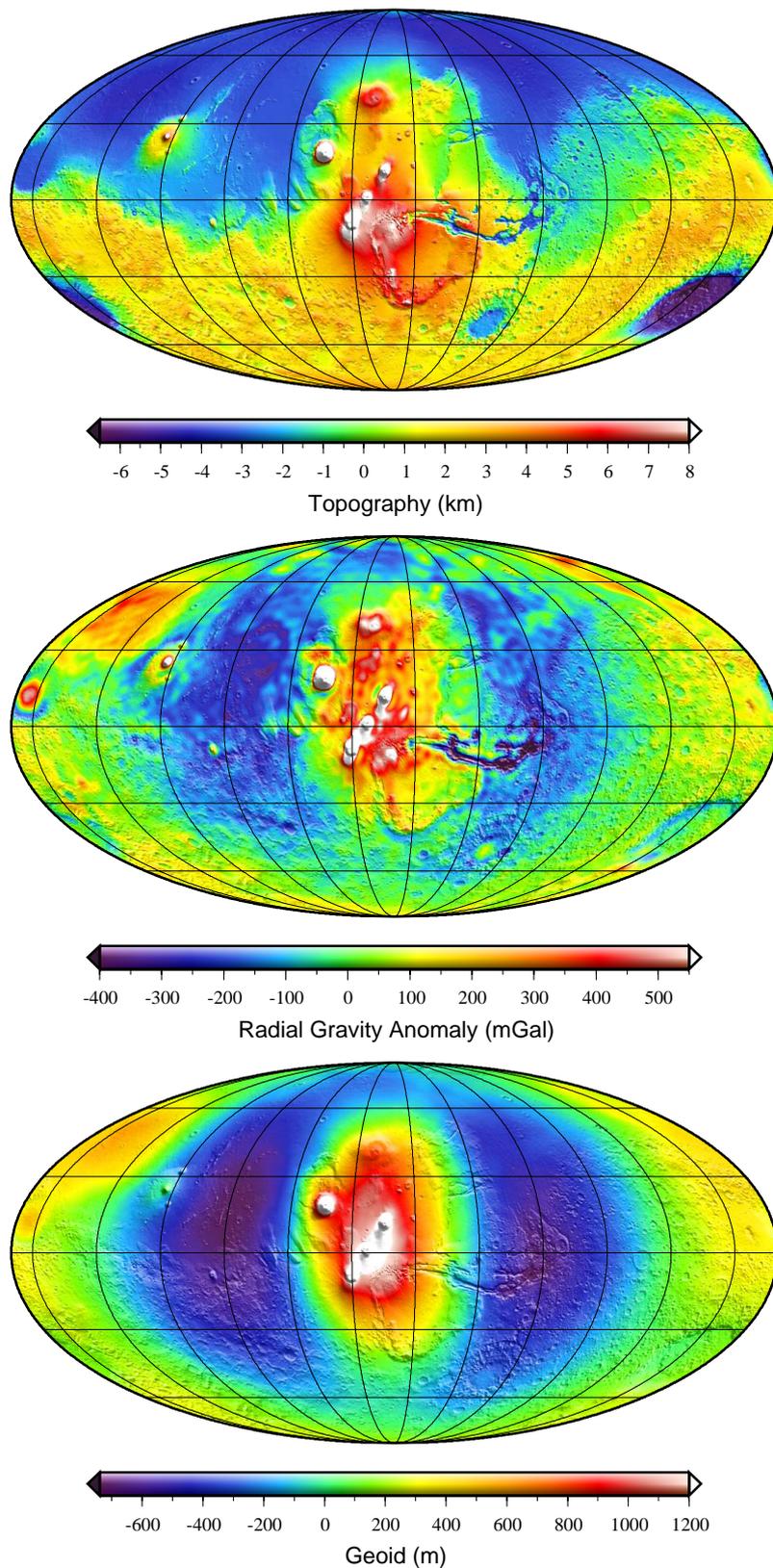
Figure 5. (top) Global topography of Mars derived from the 719-degree spherical harmonic model MarsTopo719, referenced to the geoid calculated to second order accuracy. (middle) Radial free-air gravity, evaluated at a radius of 3396 km, obtained after truncating the spherical harmonic coefficients of JGM95J01 beyond degree 75 and setting the J_2 term to zero. (bottom) First-order approximation to the geoid obtained from the same coefficients as the radial component of the gravitational field. All images are in a Mollweide projection with a central meridian of 100° W longitude and are overlain by a gradient image derived from the topography model.

offset of the center of figure from the center of mass that is directed toward 64° and S 99° W, of which the longitudinal offset is directed towards the Tharsis province. In addition to these long wavelength features, there is also an ~20 km difference between the polar and equatorial radii that is principally a result of the planet's rotational flattening.

Other major topographic features include the giant impact basins Hellas (40° S, 65° W), Argyre (50° S, 40° W) and Isidis (15° N, 85° E), the Elysium volcanic province (25° N, 145° E), the rift valley Valles Marineris, and the prominent volcanoes that are superposed on the Tharsis province. The highest elevation corresponds to the volcano Olympus Mons, which rises almost 22 km above the MOLA reference geoid.

3.3.2 Gravity

The gravitational field of Mars has been successively improved by tracking data obtained from the Mariner 9, Viking 1 and 2, Mars Global Surveyor (MGS), and Mars Odyssey missions. A major improvement in the gravity models came with the acquisition of data from the MGS mission (see *Yuan et al.* 2001; *Lemoine et al.* 2001; *Konopliv et al.* 2006). This spacecraft was in a near-polar orbit, and during the early portion of the mission when the orbit was highly elliptical, tracking data from altitudes as low as 170 km were acquired at latitudes between 60° and 85° N. Through the technique of aerobraking, the spacecraft was put into a near-circular mapping orbit with periapse and apoapse altitudes of 370 and 435 km, respectively.

The most recent and highest resolution gravity model of Mars is the JPL degree 95 model JGM95J01 (*Konopliv et al.* 2006). This model employs MGS and Mars Odyssey tracking data in combination with surface tracking data from the Pathfinder and Viking 1 landers, the latter of which were used to improve knowledge of the orientation of Mars. Some of the Mars Odyssey tracking data are from altitudes as low as ~200 km (primarily over the southern hemisphere), and aerobraking eventually put the spacecraft into a near-circular 390×455 km mapping orbit. In the absence of *a priori* constraints, inversions for the global spherical-harmonic coefficients give rise to an unrealistic power spectrum beyond degree 60. In order to obtain a higher resolution model with realistic power, the JGM95J01 model was biased towards an *a priori* power law for degrees greater than 59 by use of a Kaula rule.

An image of the radial component of the JGM95J01 gravity model is plotted in Figure 5, where the spherical-harmonic coefficients have been truncated beyond degree 75 and the J_2 term set to zero. (A small portion of the J_2 potential is likely related to the non-hydrostatic mass anomaly associated with the Tharsis bulge (e.g., *Zuber and Smith* 1997).) Clearly visible are the large positive anomalies associated with the volcanoes in the Tharsis plateau, and a negative gravity moat that surrounds this plateau (*Phillips et al.* 2001). Large positive anomalies are also evident for some of the largest impact basins, such as Isidis, Argyre, and the buried Utopia basin (45° N, 110° E) that lies in the northern plains. A negative gravitational anomaly is clearly associated with the Valles Marineris rift valley, and negative anomalies surrounding some mountains and volcanoes seem to indicate a flexural origin. Formal uncertainties in the

radial gravity are at most 10 mGal (A. Konopliv, personal communication).

The Martian geoid, as obtained from the model JGM95J01, is shown in Figure 5. The geoid undulations of Mars (after removal of the J_2 term) are seen to possess the largest amplitudes among the terrestrial planets, with a dynamic range of over 2.5 km. The signal is clearly symmetric about the Tharsis province, where a central geoid high is surrounded by an annular low. Other geoid highs are associated with the impact basins Isidis and Utopia, as well as the Elysium volcanic rise. Uncertainties in the geoid are generally no more than 2 m (A. Konopliv, personal communication).

3.3.3 Spectral Analysis

The power spectra of the Martian topography (MarsTopo719; calculated from the gridded datasets available at the PDS website) and geoid (JGMJ01) are plotted in Figure 6. In comparison to the topographic power spectrum, the Martian geoid is seen to have greater amplitudes by about two orders of magnitude than both the Earth and Venus. Furthermore, the first 5 degrees of the Martian geoid are considerably greater than would be expected based upon an extrapolation of the higher degree terms. This low-degree signal is likely a consequence of the lithospheric load and deflection associated with the Tharsis province (see *Zuber and Smith* 1997; *Phillips et al.* 2001). The error spectrum of the geoid is seen to be larger than the signal for degrees greater than ~75.

The admittance and correlation of the radial gravitational field and topography are shown in the right panel of Figure 6. The admittance function gradually increases with increasing degree, attaining a relatively constant value beyond degree 30. Beyond degree 65 both the admittance and correlation decrease as a result of the poor resolution of the gravity field. While the shape of the admittance function is somewhat similar to that of the Earth, it is important to note that the amplitudes are considerably larger at high degrees (~100 in comparison to ~35 mGal km^{-1}). Indeed, these large values are comparable to what would be expected for uncompensated topography. One apparent anomaly with the admittance spectrum is the relatively high value of 53 mGal km^{-1} for the degree three term.

With few exceptions (such as degrees 4 and 9) the correlation between the gravity and topography is also seen to be very high, with values between about 0.6 and 0.8. Similar to the Venusian gravity model, the near-sectoral terms of the Martian gravity solutions are relatively better determined because of the near-polar orbit of the MGS spacecraft. When only these near-sectoral terms are used, the correlation between the gravity and topography is considerably larger at high degrees in comparison to the case shown in Figure 6 (see *Yuan et al.* 2001; *Konopliv et al.* 2006).

3.4 The Moon

3.4.1 Topography

The topography of the Moon has been measured by several means, including satellite altimetry, stereo-photogrammetry, and radar interferometry (see *Wieczorek et al.* 2006, for a
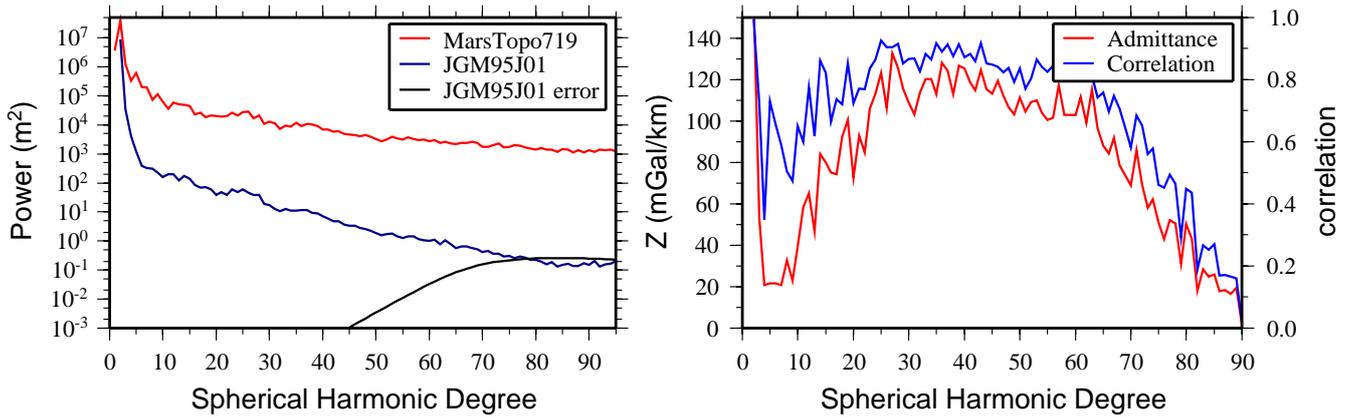
Figure 6. Power and cross-power spectra of the gravity and topography of Mars. (left) Power spectra of the topography (MarsTopo719), geoid (JGM95J01), and geoid error. (right) Admittance and correlation spectra of the radial gravity and topography.

more detailed review). However, because of the Moon's synchronous rotation, most early studies were restricted either to the nearside hemisphere, or along the equatorial ground tracks of the Apollo command and service modules. While pre-Apollo stereo-photogrammetric studies were succesful in obtaining regional topographic models with good relative precision, the long wavelength and absolute accuracies of these models were much poorer.

The Clementine mission, launched in 1994, was the first to measure absolute elevations of the lunar surface on a near global scale (see *Zuber et al.* 1994; *Smith et al.* 1997). North-south topographic profiles were obtained between 79° S and 22° N during the first month of this mission, and then between 20° S and 81° N during the second. The absolute accuracies of the obtained surface elevations are about 100 m, the cross-track orbit spacing was about 60 km at the equator, and the minimum along-track shot spacing was about 20 km (1° at the equator corresponds to 30 km). As a result of the non-optimal design of the lidar, however, the electronics often detected many returns, and these needed to be filtered to determine which, if any, were from the lunar surface. The returns from many shots were ultimately discarded, especially over the rougher highlands, leading to the acceptance of a total of 72,548 range measurements. Comparisons with a radar interferometry-derived topographic model of the crater Tycho (*Margot et al.* 1999a) suggests that a few percent of the accepted Clementine range measurements are erroneous.

As a result of the polar orbit of the Clementine spacecraft, many overlapping images exist in the polar regions under varying viewing conditions. These have been used to construct regional digital elevation models poleward of 60° having a 1-km spatial resolution (*Cook et al.* 2000; *U. S. Geological Survey* 2002). While the relative elevations obtained from these studies were tied to the Clementine altimeter data near the outer edges of these models, absolute accuracy is expected to degraded towards the poles. In particular, comparisons with independent regional models of the polar regions based on radar interferommetry data (*Margot et al.* 1999b) show differences of a kilometer or more.

The *U. S. Geological Survey* (2002) topographic model represents a combination of interpolated Clementine altimetry and elevation models of the polar regions based on stereo photogrammetry. This model is presented in Figure 7 where

it is referenced to the geoid, which includes the static gravitational model LP150Q and the rotational and tidal contributions of eq. 18. The most dramatic feature of the Moon's topography is seen to be the giant South Pole-Aitken impact basin on the southern farside hemisphere. This impact basin possesses a total relief of over 10 km, and with a diameter of over 2000 km, is the largest recognized impact structure in the solar system. Other impact basins and craters of various sizes are seen to have shaped the relief of the lunar surface, and the extensive mare basaltic lava flows on the nearside hemisphere, which are relatively younger, are seen to be comparatively smooth. Also of note is that the Moon possesses a 1.9 km displacement of its center of figure from its center of mass in the direction of 8° N and 157° W (e.g. *Smith et al.* 1997).

3.4.2 Gravity

The gravitational field of the Moon has been determined by analyses of radio tracking data of orbiting spacecraft, which include data from the Lunar Orbiter, Apollo, Clementine, and Lunar Prospector missions. While all data contribute to the lunar gravity models, by far the highest resolution constraints are obtained from the extended Lunar Prospector mission when the spacecraft altitude was lowered to approximately 30 km above the surface (for a detailed discussion, see *Konopliv et al.* 2001). However, despite this low-altitude tracking data, because of the Moon's synchronous rotation, global models of the gravitational field are severely hindered by the lack of tracking data over the lunar farside.

While spacecraft have been tracked approximately 20° over the lunar limb, there is a sizable portion of the lunar surface that lacks direct tracking constraints. Regardless, as the long term orbits of lunar satellites are influenced by gravitational anomalies that are present there, some information can be extracted over these regions when inverting the tracking data. When no *a priori* constraints are used in constructing the gravity model, the field is found to be completely unreliable in an approximately 60° radius "shadow zone" centered on the antipode of the sub-Earth point. Globally, such unconstrained models are only reliable to spherical-harmonic degree 15. In order to obtain solutions with reasonable characteristics, it is necessary to bias the spherical-harmonic co-
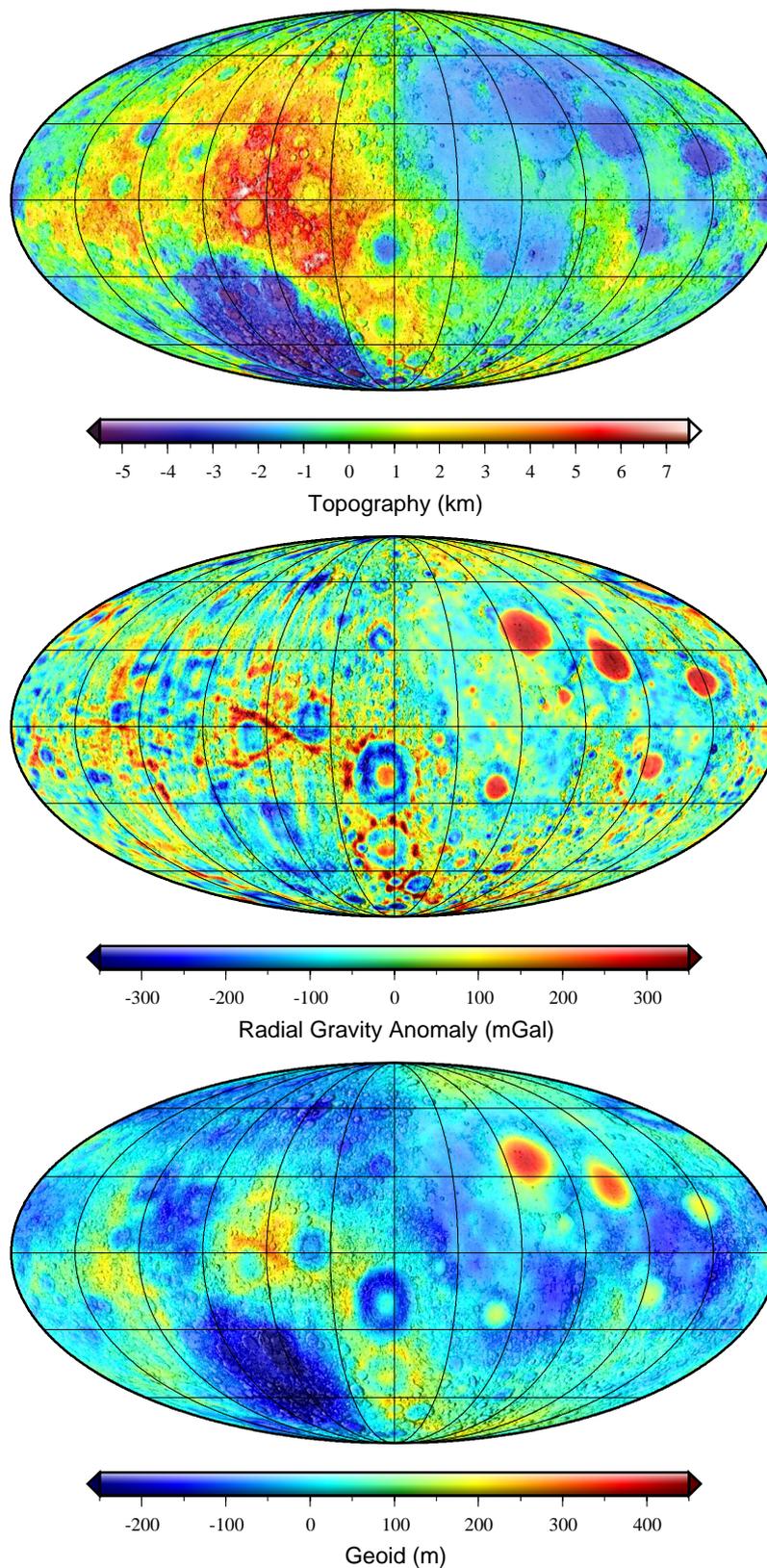
Figure 7. (top) Global topography of the Moon from the spherical harmonic model MoonUSGS359 referenced to the geoid which includes both the LP150Q gravitational model and rotational and tidal effects. (middle) Radial free-air gravity obtained from the model LP150Q evaluated at a radius of 1738 km after truncating the coefficients beyond degree 130 and setting the C_{20} and C_{22} terms equal to zero. (bottom) First-order approximation to the geoid obtained from the same coefficients as the radial gravity field. All images are in a Mollweide projection with a central meridian of 90° W longitude and are overlain by the shaded relief map of *Rosiek and Aeschliman* (2001). The near- and farside hemispheres are on the right and left halves of these images, respectively.

efficients towards an *a priori* power spectrum (i.e., by use of a "Kaula rule"). Using such methods, the most recent JPL gravity model LP150Q (*Konopliv et al.* 2001) has been determined to degree 150. Attempts to obtain regional models on the nearside with a higher resolution can be found in *Goossens et al.* (2005, in press).

The LP150Q radial gravity field of the Moon (truncated at degree 130) is plotted in Figure 7. As the equilibrium shape of a synchronously locked satellite contains both C_{20} and C_{22} terms, both of these have been removed. (While these two terms are small at the current Earth-Moon separation, it has been suggested that the Moon may posses a fossil shape that was frozen into the lithosphere early in its orbital evolution (e.g., *Jeffreys* 1976; *Lambeck and Pullan* 1980).) The major features of this map include the large positive gravitational anomalies associated with the nearside impact basins, colloquially referred to as "mascons" (e.g., *Muller and Sjogren* 1968), negative gravity moats that surround some of these basins, and the more noisy and less constrained farside field. Despite the lack of direct farside tracking data, it is remarkable that the inferred gravitational anomalies there correlate with large impact basins. Nevertheless, care should be used when interpreting these anomalies as their amplitudes could be muted, and/or their positions laterally offset. The uncertainties in the radial component of the gravitational field are estimated to be approximately 30 mGal on the nearside and can reach up to 200 mGal on the farside.

A plot of the lunar geoid is also shown in Figure 7 after removing both the C_{20} and C_{22} terms. In contrast to the Earth, which possesses maximum geoid undulations of ±100 meters, the dynamic range of the lunar geoid is more than 700 meters. When considering phenomena such as basalt flow directions, it is thus necessary to use elevations that are referenced to the full geoid. Uncertainties in the geoid are estimated to be approximately 4 meters on the nearside and 60 meters on the farside.

Finally, it is noted that the orientation of the Moon is completely described by its three principle moments of inertia, which in turn completely determine the degree-2 gravity coefficients (e.g., *Lambeck* 1988). For a synchronously rotating satellite, the minimum energy configuration is achieved when the maximum moment of inertia lies along the rotation axis, and when the minimum moment coincides with the Earth-Moon direction. A 180° rotation of the Moon about its rotation axis would be equally stable as its current configuration.

3.4.3 Spectral analysis

A spherical harmonic model of the USGS topography was developed to degree 359 and is here designated as MoonUSGS359. The power spectrum of this model, the prior model GLTM2C (*Smith et al.* 1997) that is based solely on altimetry data, and the LP150Q geoid and error are plotted in the left pane of Figure 8. Concerning the two topographic models, it is seen that the power spectra of these diverge near degree 25. Careful inspection of how these models were constructed indicates that this is a result of using different methods to interpolate the sparse Clementine data points. In comparison to the Earth, the power spectrum of the lunar geoid is seen to be at least an order of magnitude
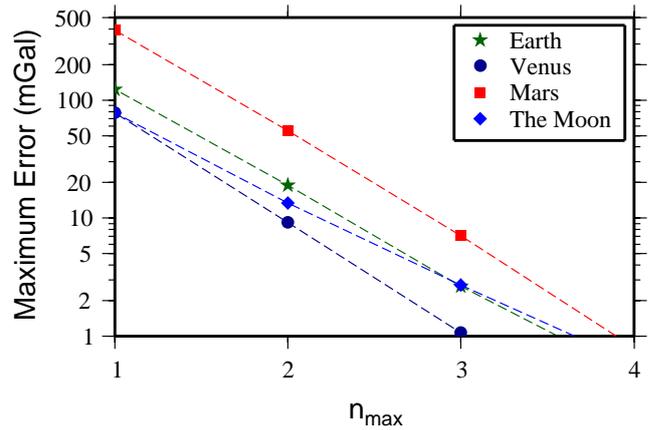

Figure 9. Maximum error associated with the Bouguer correction as a function of the order n_{max} used in eq. 30. The Bouguer correction is here defined as the radial gravitational attraction resulting from surface relief with respect to the mean planetary radius. The true value was approximated by $n_{max} = 10$, the crustal density was assumed to be 2900 kg m^{-3}, and the radial gravitational anomaly was evaluated at the maximum elevation of the planet.

more important when compared to the topography spectrum. The upturn in the geoid spectrum beyond degree 130 is a result of short-wavelength aliasing in the gravity solution, and the error spectrum of the geoid is seen to be greater than that of the geoid itself beyond degree 80. While the global harmonic coefficients should be considered unreliable beyond this degree, it should be recognized that the uncertainty in the gravity field is a strong function of position.

The correlation and admittance spectra for the gravity and topography models are plotted in the right pane of Figure 8. The curves in color represent those obtained from the model MoonUSGS359, whereas the gray curves are for the model GLTM2C. Both correlation curves show that some of the lowest degrees of the radial gravity and topography are anticorrelated. These same degrees possess negative admittance values, and this is simply a result of the presence of "mascon" impact basins, which are positive gravitational anomalies possessing low elevations. Beyond degree 25 it is seen that both the admittance and correlation spectrum obtained from the USGS model are somewhat greater than those from the GLTM2C model. While this is partially the result of the inclusions of high resolution polar topography in the USGS model, it is also likely that this is a consequence of the different interpolation schemes used in generating these models. As a decrease in correlation would be expected for a lower fidelity model, the USGS model should probably be preferred over GLTM2C. The decrease in the USGS admittance spectrum beyond degree 50 is likely to represent a loss of fidelity in both the gravitational and topographic models.

4 METHODS FOR CALCULATING GRAVITY FROM TOPOGRAPHY

Geophysical investigations that employ gravity and topography data often attempt to fit the observations with those predicted from a model that contain several parameters. For
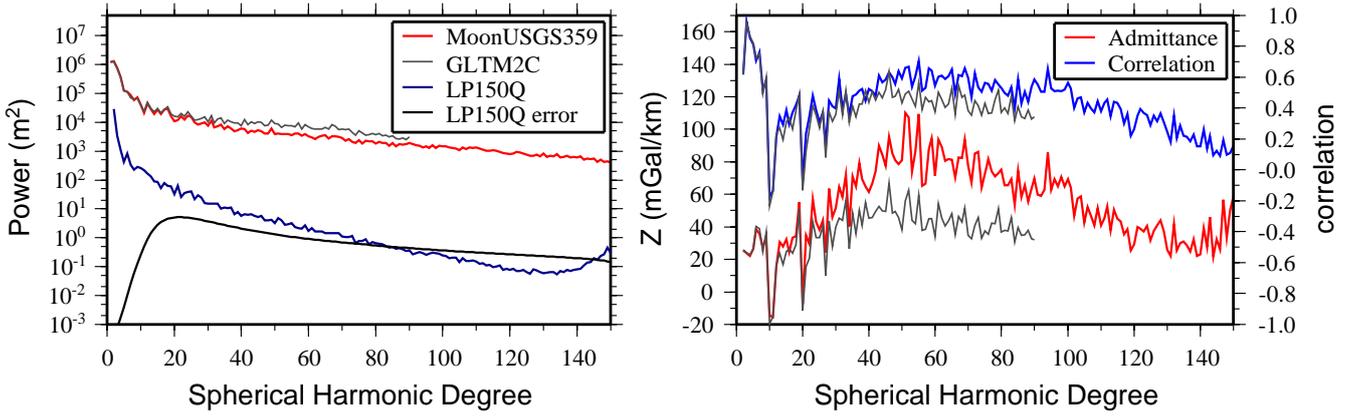
Figure 8. Power and cross-power spectra of the Moon's gravity and topography. (left) Power spectra of the topographic models MoonUSGS359 (color) and GLTM2C (gray), and the LP150Q geoid and error. (right) Admittance and correlation spectra of the radial gravity and topography using MoonUSGS359 (color) and GLTM2C (gray).

Table 2. Gravitational and shape constants.

Parameter	Value	Source
G	$6.6742(10)\ 10^{-11}\ \mathrm{m}^3\ \mathrm{kg}^{-1}\ \mathrm{s}^{-2}$	Committee on Data for Science and Technology (*Mohr and Taylor* 2005)
The Earth		
GM	$398.6004415\ 10^{12}\ \mathrm{m}^3\ \mathrm{s}^{-2}$	EGM96; *Lemoine et al.* (1998)
semi-major axis	6378.137 km	WGS84; *National Imagery and Mapping Agency* (2000)
semi-minor axis	6356.7523142 km	WGS84; *National Imagery and Mapping Agency* (2000)
radius of sphere of equal volume	6371.00079 km	WGS84; *National Imagery and Mapping Agency* (2000)
ω	$72.921150\ 10^{-6}\ \mathrm{rad\ s}^{-1}$	WGS84; *National Imagery and Mapping Agency* (2000)
Venus		
GM	$324.858592\ 10^{12}\ \mathrm{m}^3\ \mathrm{s}^{-2}$	MGNP180U; *Konopliv et al.* (1999)
Mean planetary radius	6051.878 km	VenusTopo719
ω	$-299.24\ 10^{-9}\ \mathrm{rad\ s}^{-1}$	*Konopliv et al.* (1999)
Mars		
GM	$42.828374568\ 10^{12}\ \mathrm{m}^3\ \mathrm{s}^{-2}$	JGM95I01; *Yuan et al.* (2001)
Mean planetary radius	3389.500 km	MarsTopo719
ω	$70.8821828\ 10^{-6}\ \mathrm{rad\ s}^{-1}$	*Yuan et al.* (2001)
The Moon		
GM	$4.902801076\ 10^{12}\ \mathrm{m}^3\ \mathrm{s}^{-2}$	LP150Q; *Konopliv et al.* (2001)
Mean planetary radius	1737.064 km	MoonUSGS359
ω	$2.6617073\ 10^{-6}\ \mathrm{rad\ s}^{-1}$	*Yoder* (1995)

example, lithospheric flexure calculations depend upon several unknowns, including the effective elastic thickness of the lithosphere, crustal thickness, and the density of the crust and mantle. By comparing predicted gravitational anomalies induced by the deflection of density interfaces with the observed values, the parameters of such a model can be constrained. While several methods exist for calculating the gravitational field related to relief along a density interface, as is described below, this is oftentimes most easily performed in the spherical harmonic domain.

The calculation of the gravitational potential can be considerably simplified by use of the two identities:

$$\frac{1}{|\mathbf{r} - \mathbf{r}'|} = \frac{1}{r} \sum_{l=0}^{\infty} \left(\frac{r'}{r}\right)^l P_l(\cos\gamma) \quad \text{for } r \geq r', \quad (27)$$

$$P_l(\cos\gamma) = \frac{1}{2l+1} \sum_{m=-l}^{l} Y_{lm}(\theta,\phi) Y_{lm}(\theta',\phi'), \quad (28)$$

where P_l is an unnormalized Legendre Polynomial, and γ

is the angle subtended between $\mathbf{r}$ and $\mathbf{r}'$. (Eq. 28 is commonly referred to as the Legendre addition theorem.) By inserting these equations into the expression for the gravitational potential (eq. 14), it is simple to show that the spherical harmonic coefficients of eq. 16 (the *Stokes coefficients*) are equal to

$$C_{lm} = \frac{1}{M R_0^l (2l+1)} \int_V \rho(\mathbf{r}') r'^l Y_{lm}(\theta',\phi')\, dV'. \quad (29)$$

It is important to note that this formulation of the gravitational potential can only be used when the observation point is greater than the maximum radius of the body.

Next, consider the case where there is relief $h(\theta,\phi)$ referenced to a spherical interface of radius D, and where the density ρ between h and D depends only on latitude and longitude (when h is negative, ρ is considered negative as well). For this situation, it is possible to obtain exact expressions for the corresponding potential coefficients that are similar to those developed by *Parker* (1972) in the Cartesian domain. Integrating eq. 29 over r', and expanding powers of the relief

in a Taylor series, the potential coefficients of eq. 16, referenced to a radius D, can be shown to be (see *Wieczorek and Phillips* 1998)

$$C_{lm} = \frac{4\pi D^3}{M(2l+1)} \sum_{n=1}^{l+3} \frac{(\rho h^n)_{lm}}{D^n \, n!} \frac{\prod_{j=1}^{n}(l+4-j)}{(l+3)}. \quad (30)$$

The spherical harmonic coefficients of the density multiplied by the relief to the nth power have the explicit expression (cf. eq. 8)

$$(\rho h^n)_{lm} = \frac{1}{4\pi} \int_{\Omega} [\rho(\theta,\phi) \, h^n(\theta,\phi)] \, Y_{lm}(\theta,\phi) \, d\Omega, \quad (31)$$

and when the density is constant, eq. 30 reduces to eq. 9 of *Wieczorek and Phillips* (1998). As a result of the inequality in the identity of eq. 27, this expression for the potential is only valid when the radius r is greater than the maximum elevation $D + h$. Extensions, special cases, and alternative forms of this equation have been derived independently several times in the literature (e.g., *Chao and Rubincam* 1989; *Martinec et al.* 1989; *Rapp* 1989; *Balmino* 1994; *Chambat and Valette* 2005).

For the common case where the density ρ is constant, the potential coefficients can be obtained simply by calculating the spherical harmonic coefficients of the relief to the nth power. While the sum of eq. 30 is finite, and hence exact, the number of terms grows linearly with spherical harmonic degree. Nevertheless, as each succeeding term is smaller than the previous, in paractice, this sum can be truncated beyond a maximum value $n_{\max}$ for which the truncated terms are smaller than the resolution of the gravity model.

For certain applications it is sometimes sufficient to use the first order term of eq. 30:

$$C_{lm} = \frac{4\pi D^2 (\rho h)_{lm}}{M(2l+1)}. \quad (32)$$

This expression is commonly referred to as the "mass-sheet" approximation, as the calculated gravitational anomaly would be exact if it arose from a spherical interface with a surface density of ρh. (The higher order terms are referred to as the "finite amplitude" or "terrain" correction.) Using this expression, the radial gravity (see equation 22) is seen to asymptotically approach with increasing l the Bouguer slab approximation of $2\pi\rho G h$.

The effect of truncating the sum of eq. 30 beyond $n_{\max}$ is illustrated in Figure 9 for the specific case of determining the Bouguer correction of the Earth, Venus, Mars, and the Moon. The term Bouguer correction here refers to the contribution of the gravitational potential that results from the mass between the mean planetary radius and the surface. The "true" value of the Bouguer correction was calculated using $n_{\max} = 10$, and the maximum difference in the space domain that results from truncating at lower values of n was calculated on a spherical surface corresponding to the maximum radius of the planet. As is seen, in order to obtain accuracies of a few mGal, at least the first three terms of eq. 30 are required. Utilizing only the first-order term could incur errors of a few hundred mGal for regions with high elevations.

Finally, it is noted that alternative means exist for calculating the theoretical gravitational field of a body, and that these may be preferable to the above approach for certain applications. One method developed by *Belleguic et al.* (2005) is quasi-analytic and allows for the calculation of the potential and gravity at any point in a body (this is in contrast to the above approach that is applicable only to radii greater than the maximum radius). This method starts by mapping irregularly shaped density interfaces to spherical ones, and then determines the radial derivatives of the potential and gravitational field on this surface. Using exact values for the potential and gravity field on an interface exterior to the planet (as obtained from a method similar to eq. 30), these fields are then propagated downwards using a first-order Taylor series approximation. This technique is useful for lithospheric flexure calculations as the net lithospheric load is a function of the potential at the major density interfaces.

A second method for calculating the gravitational field is based upon approximating the shape of a celestial body by a polyhedron. Exact expressions for the potential of a homogeneous polyhedron have been derived by *Werner and Scheeres* (1997), and expressions for the corresponding spherical harmonic coefficients are given in *Werner* (1997). The benefit of using this approach is that the resolution of the model (i.e., the spacing between vertices) can be varied according to the resolution of the gravitational field. An application of this method for determining the interior density of an asteroid is given by *Scheeres et al.* (2000). Alternatively, one could transform eq. 14 into a surface integral by use of Gauss' law and perform the integral numerically for a given shape model (e.g., *Cheng et al.* 2002).

5 CRUSTAL THICKNESS MODELING

It is well known that the modeling of potential fields is non-unique. For our case, eqs 16 and 32 show that any external gravitational field can be interpreted as a surface density ρh placed at an arbitrary radius D. Nevertheless, by using simplifying assumptions based on geologic expectations, it becomes possible to uniquely invert for parameters related to the interior structure of a planet.

Perhaps the simplest example of such an investigation is the construction of a planet-wide crustal thickness model. In this case, the non-uniqueness associated with potential modeling is removed by assuming that the observed gravitational field arises only from relief along the surface and crust-mantle interface (i.e., the "Moho"), and that the density of the crust and mantle are constant. It is furthermore required to assume a mean crustal thickness, or to anchor the inverted crustal thickness to a given value at a specific locale. If lateral density variations in either layer could be constrained by other means, then these could easily be incorporated into the model.

The first step is to calculate the Bouguer correction, which is the contribution to the potential of surface relief referenced to the mean planetary radius. Subtracting this from the observed gravitational field yields the Bouguer anomaly, and this is then ascribed to being caused by relief along the crust-mantle interface. To first order, this relief could be determined in the spectral domain by downward continuing the Bouguer anomaly coefficients C_{lm}^{BA} to a radius D, and then setting these equal to those predicted from the mass-sheet

approximation of eq. 32. However, two additional factors generally need to be taken into account in such an analysis. First, downward continuing the Bouguer anomaly amplifies short-wavelength noise that is often present in the observed gravitational field. Second, the first-order mass-sheet approximation may not be sufficiently accurate if the Moho undulations are large.

By minimizing the difference between the observed and predicted Bouguer anomalies, as well as an additional constraint such as the amplitude of the Moho undulations in the spectral domain, the Moho relief can be computed via the following equation (see *Wieczorek and Phillips* 1998):

$$h_{lm} = w_l \left[\frac{C_{lm}^{BA} M (2l+1)}{4\pi \Delta\rho D^2} \left(\frac{R}{D} \right)^l \right.$$

$$\left. - D \sum_{n=2}^{l+3} \frac{(h^n)_{lm}}{D^n \, n!} \frac{\prod_{j=1}^{n}(l+4-j)}{(l+3)} \right], \tag{33}$$

where $\Delta\rho$ is the density jump across the crust-mantle interface, R is the reference radius of the Bouguer anomaly coefficients, and w_l is a filter that stabilizes the downward continuation procedure. The filter w_l should be close to unity for small l, and decrease in magnitude with increasing l. While there is no simple analytic solution to this equation, the relief along the crust-mantle interface can be determined using an iterative approach: First the coefficients h_{lm} are approximated by ignoring the higher-order terms on the right-hand side, then, using this estimate, the higher-order terms are calculated, and a new estimate of h_{lm} is obtained. Examples of crustal thickness models that were obtained using this procedure are shown in Figure 10 for the Moon, Mars and Venus, and the major modeling assumptions specific to each body are described below. It is important to note that these models do not assume that the crust is isostatically compensated; such a hypothesis could be tested for a given model.

For the Moon, it is known that the mare basaltic lava flows are considerably denser than upper crustal materials (~ 3100 vs. 2800 kg m^{-3}), and that these can reach thicknesses of several kilometers within some of the largest impact basins. Thus, when computing the Bouguer anomaly for the Moon, the gravitational attraction of these must be estimated. As a result of the variable spatial resolution of the lunar gravity field, it is also necessary to apply a strong downward continuation filter (see *Wieczorek and Phillips* 1998) in order to suppress unphysical Moho undulations that arise on the farside. After truncating the potential and topography coefficients beyond degree 85, and assuming an average crustal thickness of 45 km and a mantle density of 3320 kg m^{-3}, the Moho relief was iteratively determined using eq. 33. The obtained crustal thickness model displayed in Figure 10 demonstrates that the thickness of the lunar crust could vary from approximately zero beneath some basins to more than 100 km in the highlands (see *Wieczorek et al.* 2006). Neglecting the finite amplitude terms in eq. 33 could give rise to errors as large as 20 km (*Neumann et al.* 1996).

Crustal thickness models for Mars and Venus are also presented in Figure 10. The model for Mars is an updated version from *Neumann et al.* (2004) that uses the recent JGM95J01 gravity model. For this model, the low density of the polar caps, the higher than typical densities of the Tharsis volcanoes, and the gravitational attraction resulting from the core flattening were explicitly taken into account. A mean crustal thickness of 45 km was assumed, and in downward continuing the Bouguer anomaly, a filter was constructed such that the power spectrum of the Moho relief resembled that of the surface relief. For the Venusian model, a mean crustal thickness of 35 km was assumed, the potential and topography coefficients were truncated beyond degree 60, and densities of 2900 and 3330 kg m^{-3} were used for the crust and mantle, respectively. The inclusion of finite amplitude corrections for Venus only affects the obtained crustal thicknesses by a few kilometers.

6 ADMITTANCE MODELING

In the crustal thickness modeling presented above, the non-uniqueness associated with potential modeling was removed by making certain assumptions about the mean crustal thickness and the density of the crust and mantle. These and other parameters can be estimated if one instead assumes that surface topography is supported by a specific mechanism, such as Airy compensation or lithospheric flexure. Using such a model, the relationship between gravity and topography can be determined, and by comparing to the observed values, model parameters can be estimated. As is described in the following two subsections, two methods are in common use; one is based upon modeling the geoid/topography ratio in the space domain, whereas the other models the admittance and correlation functions in the spectral domain.

6.1 Spatial domain

One method that has proven to be fruitful for estimating the mean crustal thickness of a planet is modeling of the geoid/topography ratio (GTR) in the space domain. This technique was initially developed by *Ockendon and Turcotte* (1977) and *Haxby and Turcotte* (1978) for the Earth where it was shown that the isostatic geoid anomaly was approximately equal to the vertical dipole moment of density variations within the lithosphere. For the specific cases of Airy and Pratt isostasy, the ratio between the geoid and topography was found to be proportional to the crustal thickness. This method was derived using a Cartesian geometry, and is strictly valid in the long-wavelength limit.

An alternative approach has been developed in spherical coordinates by *Wieczorek and Phillips* (1997) where it has been shown that the geoid/topography ratio can be approximated by the expression

$$\text{GTR} = R \sum_{l=l_{\min}}^{l_{\max}} W_l \, Q_l, \tag{34}$$

where $l_{\min}$ and $l_{\max}$ correspond to the minimum and maximum spherical harmonic degrees that are considered, R is the mean planetary radius, Q_l is the linear transfer function between the potential and topographic coefficients, and W_l is a weighting function that is proportional to the topographic power of degree l,

$$W_l = S_{hh}(l) \left/ \sum_{i=l_{\min}}^{l_{\max}} S_{hh}(i). \right. \tag{35}$$
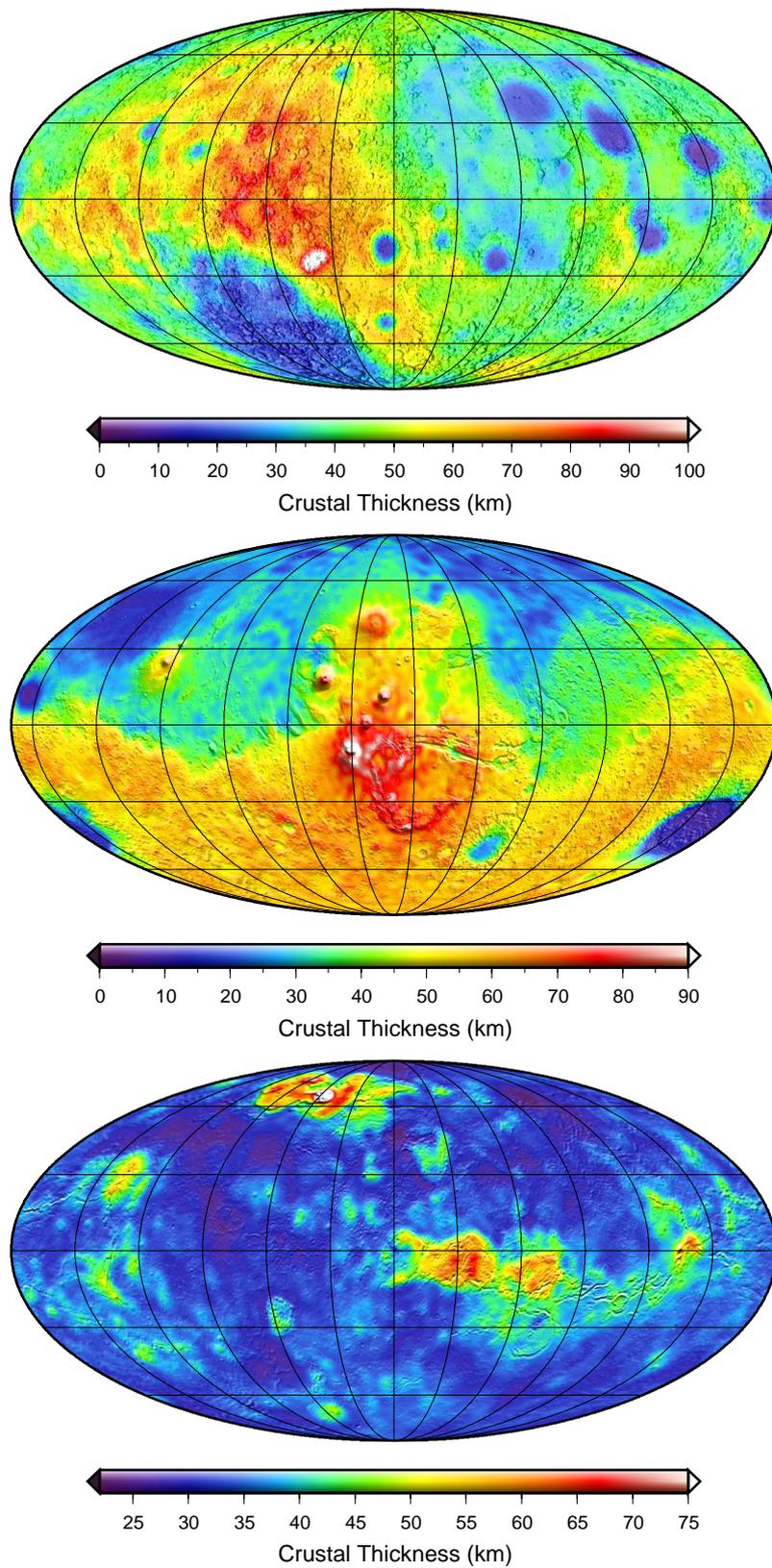
Figure 10. Crustal thickness models for the Moon (top), Mars (middle), and Venus (bottom). See sections 5 and 8 for details.

The underlying assumption of this model is that the geoid/topography ratio is independent of position for a given compensation model, and this has been empirically validated for the highlands of the Moon and Mars for the case of Airy

isostasy (*Wieczorek and Phillips* 1997; *Wieczorek and Zuber* 2004).

As the power spectra of planetary topography are "red" (i.e., they possess more power at long wavelengths than short wavelengths), eq. 35 shows that the largest contribution to the geoid/topography ratio will inevitably come from the lowest degrees. As an example, approximately 80% of the GTR for the Moon is determined by degrees less than 30. As the topography of the ancient highland crust of a planet is likely to be isostatically compensated at these wavelengths, it is common to employ a model based on the condition of Airy isostasy for these regions. Assuming that the density of the crust is constant, and using the condition of equal mass in crust-mantle columns, it is straightforward to show using eq. 32 that the transfer function between the potential and topographic coefficients is

$$Q_l = \frac{C_{lm}}{h_{lm}} = \frac{4\pi \rho_c R^2}{M(2l+1)} \left[1 - \left(\frac{R - T_c}{R} \right)^l \right], \quad (36)$$

where ρ_c is the density of the crust, and T_c is its mean thickness.

In practice, the geoid/topography ratio is determined by fitting the observations to a straight line within a region that is believed to be consistent with the employed model. By utilizing a plot of the predicted GTR vs. T_c (obtained from eqs 34–36), the crustal thickness can then be estimated for a given value of ρ_c. Nevertheless, as the GTR is heavily influenced by the longest wavelength components of the gravity and topography, several aspects need to be carefully considered when performing such an analysis.

It is first necessary to ensure that the entire signal of the geoid and topography are governed by the same compensation model. While this can never be entirely satisfied, certain anomalous long-wavelength features can sometimes be identified and removed. For instance, most planets and satellites possess significant rotational and/or tidal contributions to their degree-2 shape, and these signatures can be minimized by setting these coefficients to zero. For Mars, in addition to the degree-2 rotational signature, the longest wavelength components have been affected by the load and flexural response associated with the Tharsis province (see *Zuber and Smith* 1997; *Phillips et al.* 2001; *Wieczorek and Zuber* 2004). Furthermore, as the degree-1 potential terms are zero when the gravitational field is referenced to the body's center of mass, any degree-1 topography that exists may need to be treated separately. Finally, as the GTR is largely determined by the longest wavelength components of the geoid and topography, it is necessary that the region of interest be sufficiently large when regressing the geoid and topography data.

6.2   Spectral domain

Two major shortcomings associated with modeling the geoid/topography ratio are that only a single wavelength-independent parameter is used (the GTR) and the observed value could be biased by long-wavelength features that are unrelated to the assumed compensation model (such as lateral density anomalies in the mantle caused by mantle convection). An alternative modeling approach that largely by-passes these concerns is to model the relationship between
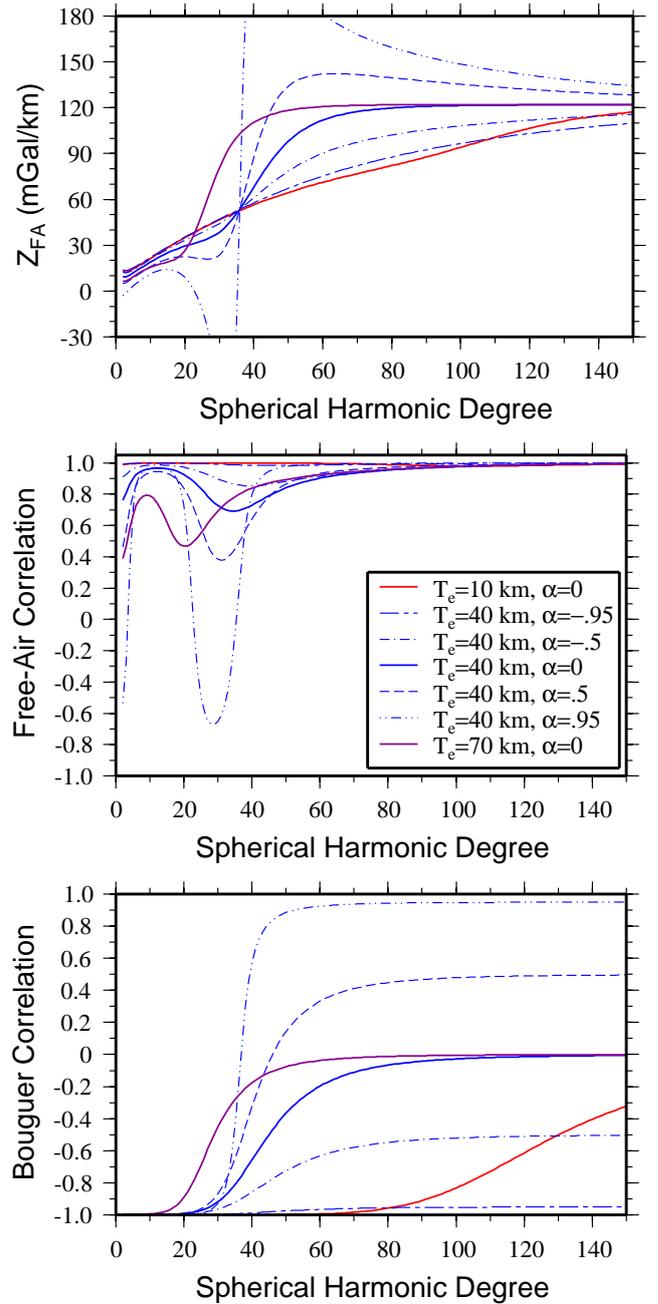

Figure 11. (top) Free-air admittance, (middle) free-air correlation, and (bottom) Bouguer correlation, for a flexural model with equal magnitudes of applied surface and subsurface loads. Model parameters correspond to the planet Mars, with $T_c = z = 50$ km, $\rho_c = 2900$ kg m^{-3}, $\rho_m = 3500$ kg m^{-3}, and $E = 10^{11}$ Pa. Solid lines correspond to the case where the applied surface and subsurface loads have random phases (i.e., $\alpha = 0$), and the dashed lines correspond to the case where these loads are partially correlated.

the gravity and topography for a certain region in the spectral domain. As wavelength-dependent admittance and correlation functions are obtained, in principle, it is possible to invert for several model parameters. The major shortcoming is that the resolution of the gravity and topography becomes increasingly poor with increasing degree l. This section describes the basic concepts involved with such a spectral anal-

ysis applied on a global scale. In section 7, the technique of obtaining localized spectral estimates will be described.

Let us presume that the potential and topography coefficients are related via an equation of the form

$$C_{lm} = Q_{lm} h_{lm} + I_{lm}, \tag{37}$$

where Q_{lm} is a linear non-isotropic transfer function, and I_{lm} is that portion of the potential not described by the model. For simplicity, it will be assumed that I_{lm} is zero (though this assumption will be relaxed later) and that the topography is noise free. Though the above relationship is inherently non-isotropic, it is often useful to work with the power and cross-power spectra of the gravitational field and topography, S_{hh}, S_{gg} and S_{hg}, which only depend upon spherical harmonic degree l. The goal is to fit these three functions to those obtained from an appropriate model. In order to remove the model dependence of certain nuisance parameters, it is convenient to work with ratios of these three (cross-)power spectra. Although several such ratios involving powers of these are possible, only two will be independent, and it is traditional to use the admittance and correlation spectra as previously defined by eqs 25 and 26. If a model describing a planet's gravity and topography is to be considered successful, then it must satisfy both of these functions. If one or both of these functions can not be fit for a given degree, then this is a clear indication that either the model assumptions are inappropriate for the region being investigated, or the input data sets are not sufficiently accurate.

If one treats the lithosphere of a planet as a thin elastic spherical shell overlying a fluid interior (see *Kraus* 1967), then a simple relationship exists in the spectral domain between the load on the lithosphere and its deflection (see *Turcotte et al.* 1981; *Willemann and Turcotte* 1981; *Banerdt* 1986). If loading at only a single interface is considered (either at or below the surface), then the transfer function in eq. 37 is isotropic (i.e., independent of m). For this situation, expressions for the admittance and correlation functions can be schematically written as:

$$Z(l) = f\left(\rho_c, \rho_m, \nu, E, T_e, T_c, z, g, R\right), \tag{38}$$
$$\gamma(l) = 1 \quad \text{or} \quad -1, \tag{39}$$

where f denotes a functional dependence on the enclosed parameters. In particular, the admittance function explicitly depends on the crustal and mantle density, Poisson's ratio ν, Young's modulus E, the elastic thickness T_e, the crustal thickness, the depth of the load z, the magnitude of the gravitational acceleration g, and the radius of the planet. For an isotropic transfer function Q_l, it is trivial to show that the degree-correlation function (in the absence of noise) is equal to the sign of Q_l. This model has been amended by *McGovern et al.* (2002) and *Belleguic et al.* (2005) to include in-phase loads applied to and below the surface when the two are linearly related by a degree-independent constant. Such models would include an additional parameter L, which is a function of the relative magnitudes of the surface and subsurface loads. Geologic situations where surface and subsurface loads might be perfectly correlated include isolated volcanoes and impact basins.

An alternative loading model that includes loads applied to and below the surface was developed by *Forsyth* (1985) in the Cartesian domain (see also *Banks et al.* 2001). In contrast to models that take the applied loads to be perfectly in phase, he assumed that the phase differences of the applied surface and subsurface loads were random. Such an assumption might be expected to be reasonable for continental cratons where several geologic processes have operated over extended periods of time (such as erosion, sedimentation, and magmatism). In contrast to eq. 39, this model possesses a wavelength-dependent correlation function. A model similar to that of *Forsyth* (1985) has been derived in spherical coordinates by *Wieczorek* (manuscript in preparation), and can be schematically described by the following equations:

$$Z(l) = f\left(\rho_c, \rho_m, \nu, E, T_e, T_c, z, L, \alpha_l, g, R\right), \tag{40}$$
$$\gamma(l) = f'\left(\rho_c, \rho_m, \nu, E, T_e, T_c, z, L, \alpha_l, g, R\right), \tag{41}$$

where both f and f' represent generic functional dependencies. As an extension to *Forsyth*'s model, this formulation allows for an arbitrary phase relationship between the applied surface and subsurface loads that is described by the additional parameter α, which can possess values between 1 and -1. The expectation of this function is given by the expression

$$\alpha_l = \frac{\sum_{m=-l}^{l} \langle \cos \Delta_{lm} \rangle}{(2l + 1)}, \tag{42}$$

where Δ_{lm} denotes the phase difference between the two loads, and $\langle \cdots \rangle$ is the expectation operator. For random phases, α is zero, and the model degenerates to that of *Forsyth* (1985). When the loads are perfectly in or out of phase by 0 or 180°, $\alpha = \pm 1$ and the model is analogous to that of *McGovern et al.* (2002) and *Belleguic et al.* (2005).

Examples of the predicted free-air admittance and correlation functions are shown in Figure 11 for several values of the elastic thickness and phase parameter α. These models were generated using parameters typical for the planet Mars, and the magnitudes of the applied surface and subsurface loads were chosen to be equal. As is seen, these curves are strong functions of both the elastic thickness and α, and by considering both the admittance and correlation, it may be possible to separate the effects of the two. The free-air correlation function is seen to possess low values over a restrictive range of wavelengths that is diagnositic of the elastic thickness. Furthermore, the free-air correlation function is seen to approach unity at large degrees ($l \gtrsim 100$). In practice, if a decline of the free-air correlation is observed with increasing degree, this is usually a good indicator of a loss of fidelity with the employed gravitational model. The predicted Bouguer correlation function is also shown for the same model parameters, and this shows a behavior similar to that predicted by *Forsyth*'s model. In particular, it is noted that the Bouguer correlation asymptotically approaches the value of α with increasing degree. While the Bouguer correlation is useful for interpretive purposes, its use is not advocated here because the Bouguer gravitational anomaly critically depends upon the value chosen for the crustal density, and this is generally not known *a priori*.

The preceding discussion explicitly assumed that the unmodeled gravitational signal I_{lm} in eq. 37 was identically zero. As mentioned in section 2.2, if I_{lm} and the topography are uncorrelated, the expectation of the admittance will not be affected by the presence of such a signal. However, the expectation of the gravitational power spectrum will be biased upwards by an additive constant S_{II}, and this

will tend to bias the correlation function downwards. Fortunately, any theoretical loading model can be easily modified to incorporate an unmodeled signal I_{lm} that is uncorrelated with the topography: All one needs to do is add a degree-dependent constant S_{II} to the theoretically predicted gravitational power spectrum (see eq. 24). It would be a simple matter to include S_{II} as an inversion parameter in a generic loading model such as eq. 41, though it is noted that this has not yet been attempted. While I_{lm} is commonly assumed to be gravitational measurement noise, this need not be the case. As described by *McKenzie* (2003), massive erosion and/or sedimentation of a lithosphere possessing surface and subsurface loads could give rise to a final state where the surface is perfectly flat, but where gravitational anomalies are present. If this final state were taken as the initial condition of a *subsequent* loading event, then the initial gravitational signature (which is unrelated to the second loading model) would be expected to be uncorrelated with the subsequently generated topography.

Finally, it is important to re-emphasize that if a given model of lithospheric loading is an accurate description of reality, it must fit both the admittance and coherence functions. If this can not be done, then either the model or data must be inaccurate. Unfortunately, the vast majority of published investigations that use Forsyth-like loading models employ only the admittance or coherence function. The values of inverted parameters from such studies, while perhaps correct, need confirmation by analysis of the other function. Notable exceptions include the papers by Forsyth and coworkers (*Forsyth* 1985; *Bechtel et al.* 1987; *Ebinger et al.* 1989; *Bechtel et al.* 1990; *Zuber et al.* 1989), *Phillips* (1994), and *Pérez-Gussinyé et al.* (2004). Similarly, many published investigations that employ a loading model with only surface or subsurface loads also ignore the correlation function, even though such models explicitly require this to be ± 1 when I_{lm} is zero. Nevertheless, it must be noted that no published study has yet attempted to fit both the admittance and correlation functions simultaneously when an unmodeled gravitational signal is present that is uncorrelated with the topography.

7   LOCALIZED SPECTRAL ANALYSIS

As the spherical harmonics are global basis functions, the power spectrum as defined by eq. 9 is necessarily representative of the global properties of the function. In geophysics, however, it is reasonable to suspect that the spectral properties of the gravity and topography will vary as a function of position. For example, the elastic thickness may differ among geologic provinces as a result of their unique histories. Alternatively, it might arise that the data are only locally known, and that one would like to estimate the power spectrum based exclusively upon these data.

One way of obtaining localized estimates of a function's power spectrum is to first multiply the data by a localizing window (commonly referred to as a data taper), and then to expand this windowed function in spherical harmonics (for a detailed discussion in the Cartesian domain, see *Percival and Walden* 1993). However, as a result of the windowing procedure, the resultant power spectrum will differ from the true value. For the case where the input field is stationary,
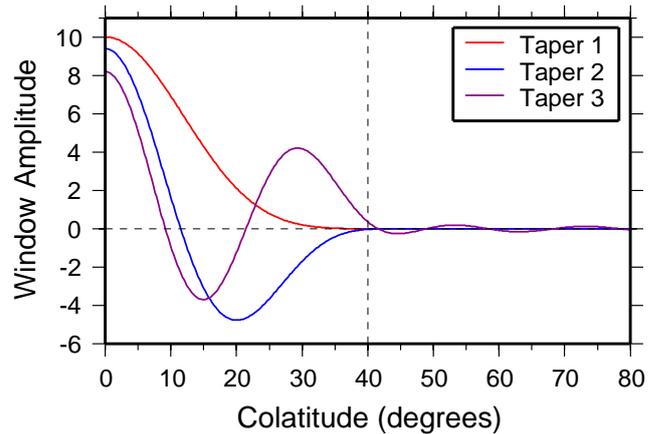

Figure 12. The first three zonal data tapers, bandlimited at $L = 17$, whose power is optimally concentrated within colatitudes less than $40°$. The space-bandwidth product N_0 is here equal to 4.

and the spherical harmonic coefficients are governed by a zero-mean stochastic process, it can be shown that the expectation of the windowed power spectrum is related to the global spectrum by the following relation (*Wieczorek and Simons* 2005, 2007):

$$\langle S_{\Phi\Gamma}(l) \rangle = \sum_{j=0}^{L} S_{hh} \sum_{i=|l-j|}^{l+j} S_{fg}(i) \left(C_{i0j0}^{l0} \right)^2. \tag{43}$$

Here, h represents an arbitrary window bandlimited to degree L, Φ and Γ are the windowed fields hf and hg, respectively, and the symbol in parenthesis is a Clebsch-Gordan coefficient (these are related to the Wigner 3-j symbols and are proportional to the integral of three Legendre functions, see *Varshalovich et al.* (1988)). The expectation of the windowed power spectrum $S_{\Phi\Gamma}$ is seen to be related to the global spectrum by a smoothing operation reminiscent of a convolution.

For a localized spectral analysis, the question naturally arises as to what form the localizing window should take. In order to localize the data, it is clear that the amplitude of the window (or its power) should be near zero outside the region of interest. Furthermore, as a result of the convolution-like relationship between the global and windowed spectra, the bandwidth L of the window should be as small as possible in order to limit this spectral smoothing. Slepian and coworkers (see *Slepian* 1983) previously posed and solved this problem in Cartesian geometry by finding those windows whose power were optimally concentrated in a specified region. Using this same criterion, *Wieczorek and Simons* (2005) and *Simons et al.* (2006) solved for those bandlimited windows on the sphere that are optimally concentrated for all colatitudes less than θ_0. This optimization problem reduces to a simple eigenvalue equation whose solution yields a family of orthogonal data tapers; the quality of the concentration is given by the corresponding eigenvalue. For the case of zonal functions, it was shown that the properties of these windows depend almost exclusively on the space-bandwidth product

$$N_0 = (L+1)\frac{\theta_0}{\pi}, \tag{44}$$

and that the first $N_0 - 1$ windows were near optimally con-

centrated. As an example, the best three concentrated windows corresponding to $\theta_0 = 40°$, $N_0 = 4$, and $L = 17$ are plotted in Figure 12. The number of well concentrated windowing functions can be dramatically increased by making use of the non-zonal tapers (*Wieczorek and Simons* 2007). The extension of this method to arbitrarily-shaped concentration regions is given by *Simons et al.* (2006).

While a method had previously been used in spherical coordinates where a function is multiplied by a single localization window (*Simons et al.* 1997), the use of multiple tapers, as originally pioneered by *Thomson* (1982) in the Cartesian domain, has several key advantages. First, while the energy of any single window will non-uniformly cover the concentration region, the cumulative energy of orthogonal tapers is nearly constant for the region of interest. Thus, an average of spectra obtained from several orthogonal tapers will be more representative of the data than that of a single taper. Second, while it is generally not possible to obtain the expectation of the localized spectrum since there is generally only a single field available for analysis, the spectral estimates obtained from orthogonal tapers are nearly uncorrelated, and their average can be considered as an approximation of the expectation. Finally, by using multiple tapers, it is possible to make an estimate of the uncertainty associated with a given spectral estimate; this is expected to decrease as approximately $1/\sqrt{N}$ where N is the number of tapers (*Wieczorek and Simons* 2005, 2007).

In performing a localized spectral analysis, there are several factors that need to be considered. First, it is noted that if the fields f and g of eq. 43 are only known to a maximum spherical harmonic degree L_{fg}, then only the first $L_{fg} - L$ windowed spectral estimates are reliable. Second, those localized spectral estimates with degrees less than L are heavily biased and possess relatively large uncertainties, making these of little use for geophysical analysis. Third, while a multitaper spectral analysis is generally preferable to using a single taper, the above two concerns present serious limitations when working with the relatively low resolution gravity fields of Venus, Mars and the Moon. Depending on the size of the concentration region, it may be infeasible to use the larger bandwidths that are required for obtaining several well concentrated tapers.

Finally, when comparing model results to observations, it is emphasized that the two must be windowed in the same manner (e.g., *Pérez-Gussinyé et al.* 2004). If the analysis is performed by generating forward models of the gravity field using the known topography, then it is only necessary to localize these functions in the same manner as the data. Alternatively, if no explicit expression exists for Q_{lm} (as in the model of *Forsyth* (1985) and that presented in section 6.2, both of which are statistical in nature), then it is necessary to window the predicted (cross-)power spectra using eq. 43 before calculating the theoretical admittance and correlation functions (for the Cartesian analog, see eq. 4.2 of *Thomson* 1982).

8 SUMMARY OF MAJOR RESULTS

8.1 The Earth

The gravity and topography of the Earth have been used extensively to decipher the rheological properties of the crust and upper mantle. The literature is voluminous, and the reader is referred to several reviews in volume 8 of this series, *Watts* (2001), and the references in the papers cited below. Here, only a few subjects will be touched upon that bear relevance to investigations of Venus, Mars, and the Moon. These include modeling of the elastic thickness of the oceanic and continental lithosphere, inelastic flexural modeling, and the modeling of dynamic topography and geoid signatures associated with mantle convection.

Flexural modeling of the oceanic lithosphere is relatively simple in that loading is primarily a result of the construction of isolated shield volcanoes. Elastic thickness estimates have been obtained by modeling the topographic and gravity signatures of these features, and it is widely accepted that the elastic thickness is primarily dependent upon the age of the plate at the time of loading, with T_e being generally less than about 45 km (for a review, see *Watts* 2001). In particular, a plot of the elastic thickness versus age of the lithosphere at the time of loading resembles the time dependence of the depth to an isotherm ($\sim$300–600 °C) predicted from a plate cooling model (see *Watts and Zhong* 2000). This suggests that the flexural signature has been "frozen" into the lithosphere as it cooled and that long term viscoelastic relaxation has been relatively unimportant. Nevertheless, a description of the initial short-term subsidence of the lithosphere (i.e., the first few 10s of ka) requires the use of a viscoelastic model, and given the relatively restricted age range of oceanic lithosphere ($<$200 Ma), it is difficult to discern if viscoelastic relaxation would be important at longer timescales. It is important to note that most flexural modeling of features on the other terrestrial planets has been for loads that were emplaced on the lithosphere over a billion years ago.

Investigations of the continental elastic thickness have been more contentious. Part of the difficulty arises because it is not clear *a priori* as to the importance of subsurface loading and the phase relationship of the surface and subsurface loads (see section 6.2). A loading model was developed by *Forsyth* (1985) that took into account both surface and subsurface loading under the assumption that the two were uncorrelated, and application of this method has yielded elastic thicknesses in the broad range of 5–134 km (*Forsyth* 1985; *Bechtel et al.* 1987; *Ebinger et al.* 1989; *Bechtel et al.* 1990; *Zuber et al.* 1989; *Pérez-Gussinyé et al.* 2004). There is currently some controversy as to whether the values greater than $\sim$25 km are reliable (compare *McKenzie* (2003) with *Watts and Burov* (2003)), but this debate will not be definitively settled until investigators fit both the admittance and correlation functions simultaneously while taking into account the presence of an unmodeled gravitational signal that is uncorrelated with the topography (see section 6.2). Furthermore, with the exception of *Pérez-Gussinyé et al.* (2004), all studies that have inverted for the elastic thickness using multitaper spectral analysis techniques have done so using a methodology that is not entirely correct. In particular, the windowed power spectra from a multitaper analysis represent a convolution of the true power spectra with that of the

window (see eq. 4.2 of *Thomson* 1982). Thus, it is necessary to convolve the theoretical (cross-)power spectra with that of the data tapers before obtaining theoretical windowed admittance and coherence functions. Regardless, application of the multitaper method has convincingly shown that the elastic thickness of some continental regions is not always isostropic (e.g., *Simons et al.* 2000, 2003), which is an assumption common to most studies.

While the majority of investigations that model flexure of the lithosphere assume that it is perfectly elastic, elastic stresses are often predicted to be in excess of the strength of geologic materials. A simple modification to the elastic flexure equation that takes this into account is to replace the elastic bending moment-curvature relationship with one that is based upon an elastic-perfectly plastic (EP) model of the lithosphere's yield strength (e.g., *Burov and Diament* 1995; *Mueller and Phillips* 1995). Here, the strength of the upper crust is limited by brittle failure, and stresses in the lower crust and mantle are limited by their ductile strength for a specified strain rate. Predicted flexural profiles are time-invariant and can sometimes differ significantly from those of the perfectly elastic model. As the ductile strength is temperature dependent, these results are sensitive to the assumed lithospheric temperature gradient.

A more realistic model of lithospheric deformation uses a time-dependent elastoviscoplastic (EVP) formulation (e.g., *Albert and Phillips* 2000; *Albert et al.* 2000; *Brown and Phillips* 2000). The main advantage of these models is that the strain rates are explicitly calculated, as opposed to assumed as in the EP models. While the best-fit EP and EVP flexural profiles can be quite similar, it is not clear *a priori* how one should estimate the characteristic strain rate that is required for the EP model without running a full EVP simulation (*Albert et al.* 2000). The EVP models show that significant decoupling of stresses may occur between the crust and mantle if the lower crust is sufficiently weak (e.g., *Brown and Phillips* 2000). When this occurs, the effective elastic thickness decreases; the exact value is highly dependent upon the crustal thickness, load magnitude, and assumed rheology of the crust and mantle. In constrast, when the lower crust is strong, the maximum achievable effective elastic thicknesses are consistent with the depth of an $\sim$700 °C isotherm obtained from a lithospheric cooling model. Flexural modeling of a volcano growing on a cooling lithosphere shows that the effective elastic thickness is "frozen" into the lithosphere shortly after volcanic construction is complete (*Albert and Phillips* 2000).

Finally, in addition to near-surface crustal thickness and density variations, significant gravity and topography signatures can be generated by dynamic processes in the mantle, such as beneath hot spots and subduction zones. While there are few, if any, convincing examples of plate subduction on the other terrestrial planets, hot spots similar to the Earth are believed to exist on both Venus and Mars. Dynamic modeling of plumes shows that the major variable controlling the surface gravity and topography signatures is the depth dependence of the mantle viscosity. In the absence of a shallow low viscosity asthenosphere, convective stresses generated at depth are efficiently coupled to the surface, generating large signals and large corresponding effective depths of compensation. However, the inclusion of a shallow low viscosity zone can significantly reduce these signatures, and apparent depths of compensation are found to be significantly shallower (e.g., *Robinson and Parsons* 1988; *Ceuleneer et al.* 1988). Joint inversions utilizing mantle density anomalies from seismic tomography and estimates for the dynamic topography signal imply the existence of a low-viscosity zone somewhere in the upper mantle, and a gradual increase in viscosity with depth by an order of magnitude in the lower mantle (e.g., *Panasyuk and Hager* 2000).

8.2 Venus

Our knowledge of Venus has dramatically improved since the acquisition of gravity, topography, and SAR imagery by the Magellan mission between 1990 and 1994. While the size and bulk density of Venus were known beforehand to be similar to that of the Earth, this planet was found to differ dramatically in that it lacks any clear sign of plate tectonics. A major unanswered question is how this planet loses its internal heat, and whether or not this process is episodic or uniform in time. Geophysical analyses have been used to constrain the crustal and elastic thickness, and the latter has been used to place constraints on the temperature gradient within the lithosphere. Reviews concerning the geophysics of this planet can be found in *Phillips et al.* (1997), *Grimm and Hess* (1997), *Schubert et al.* (1997), and *Nimmo and McKenzie* (1998).

The crustal plateaus of Venus generally have low-amplitude gravitational and topographic signatures within their interiors and are potential candidates for being isostatically compensated (one notable exception is Ishtar Terra). By assuming that the surface topography is compensated at a single interface, *Smrekar and Phillips* (1991) obtained best-fit apparent depths of compensation (ADCs) between 50 and 90 km by modeling Pioneer Venus line-of-sight gravity data over Gula, Ovda, Phoebe, Tellus, Thetis and Ulfrun Regiones. Using higher resolution Magellan data *Grimm* (1994) obtained best-fit ADCs between 20 and 50 km for Alpha, Tellus, Ovda, and Thetis Regiones. These values are plausibly interpreted as representing the crust-mantle interface, especially when considering that the crustal thickness at the mean planetary radius would be thinner given the high average elevations associated with the above study regions. An analysis of geoid/topography ratios by *Kucinskas and Turcotte* (1994) found zero-elevation crustal thickness of 50±7 and 65±13 km for the crustal plateaus of Ovda and Thetis Regiones, respectively, consistent with the above mentioned studies. *Moore and Schubert* (1997) similarly found values 44±4, 83±8, 75±17, and 75±22 km for Alpha, Ovda, Tellus, and Thetis Regiones, respectively. (These latter estimates might overestimate the zero-elevation crustal thickness as regional low-pass filtered versions of the gravity and topography were removed before performing the regression.) If any portion of the geoid and topography were to result from Pratt or thermal compensation, the obtained crustal thicknesses would represent an upper bound. A spectral admittance study by *Phillips* (1994) (described below) obtained a slightly thinner crustal thickness of 30±13 km for the region of Atla Regio (updated to 38±9 km in *Phillips et al.* (1997)).

An addition constraint concerning the thickness of the Venusian crust is related to its compositional buoyancy. In particular, if the crust were basaltic in composition, then

this material should undergo a phase transition at high pressure to the more dense mineral assemblage of eclogite (e.g., *Grimm and Hess* 1997). This material could potentially delaminate from the crust as a result of its high density, and the depth of this phase transition might thus constrain the maximum achievable crustal thickness. For a MORB composition, the eclogite phase transition is predicted to occur at depths of ∼70 to 120 km (see *Ghent et al.* 2004) for linear temperature gradients of 5 and 15 K km^{-1}, respectively. Inspection of the crustal thickness map in Figure 10 (which is based upon the premise of an average crustal thickness of 35 km) shows that crustal thicknesses near 70 km exist only in the highland plateaus of Ishtar Terra, and Ovda and Thetis Regiones, suggesting that crustal delamination could have occurred in these regions. If this crustal thickness map is an accurate representation of reality, it is curious that the highland crust is almost exactly twice as thick as the lowland crust; this potentially could arise by the obduction of one plate over another.

In contrast to the majority of the highland plateaus, large apparent depths of compensation and geoid/topography ratios have been found for the the volcanic rises (*Smrekar* 1994; *Kucinskas and Turcotte* 1994; *Moore and Schubert* 1995, 1997) and Ishtar Terra (*Grimm and Phillips* 1991; *Hansen and Phillips* 1995; *Moore and Schubert* 1997). Such values are not consistent with compensation occurring solely by crustal thickening, but require either some form of dynamic support from the mantle via stresses induced by ascending mantle plumes (e.g., *Vezolainen et al.* 2004), and/or substantial thinning of a thick (∼300 km) thermal lithosphere (*Kucinskas and Turcotte* 1994; *Moore and Schubert* 1995, 1997). If a low viscosity asthenosphere were present at shallow mantle depths, as is the case of the Earth, the predicted GTRs and ADCs resulting from dynamic support would be considerably smaller than measured as a result of the decoupling of stress between the lithosphere and mantle (e.g., *Kiefer et al.* 1986; *Kiefer and Hager* 1991). These results seem to imply that in contrast to the Earth, Venus lacks a low viscosity zone, which is most likely a result of a volatile-poor mantle. A strong coupling of stresses between the lithosphere and mantle is the likely cause of the high spectral correlation between gravity and topography for the lowest spherical harmonic degrees of Venus (contrast Figures 2 and 4).

Elastic thickness estimates have been obtained for a variety of features based exclusively on topographic profiles that are indicative of flexure. The benefit of using topography alone is that small features can be investigated that are not resolved in the current gravity model. Elastic thicknesses of 11–25 km have been obtained by modeling the Frejya Montes foredeep (*Solomon and Head* 1990; *Sandwell and Schubert* 1992), and ∼10–60 km for potential flexural buldges outboard of coronae (*Sandwell and Schubert* 1992). Additional features modeled by *Johnson and Sandwell* (1994) yield elastic thicknesses of 10–40 km, and potential subduction related sites possess a range of 6–45 km (*Schubert and Sandwell* 1995). Predicted stresses are largest where the plate curvature is greatest, and faulting is generally visible in the Magellan SAR imagery at these locations. Modeling by *Barnett et al.* (2002) yielded best-fit elastic thicknesses that are consistent with the above studies. Modeling the location of concenctric faulting around Nyx Mons

(a volcano in Bell Regio) implies a best-fit elastic thickness of ∼50 km (*Rogers and Zuber* 1998). It is important to note that the assumption of a perfectly elastic rheology may be grossly inappropriate for some features. For instance, the magnitude of the flexure-induced bulge south of Artemis Chasma implies that significant yielding has occurred within the lithosphere, and inelastic modeling by *Brown and Grimm* (1996) shows that a significant compressive in-plane force is required at this locale.

The elastic thickness has also been estimated for various regions of Venus through a combined analysis of gravity and topography data in the spectral domain. Unfortunately, with the exception of one study, these investigations have only fit the admittance or coherence functions, but not both simultaneously (e.g., *McKenzie* 1994; *Smrekar* 1994; *Simons et al.* 1994, 1997; *McKenzie and Nimmo* 1997; *Smrekar and Stofan* 1999; *Barnett et al.* 2000, 2002; *Lawrence and Phillips* 2003; *Smrekar et al.* 2003; *Hoogenboom et al.* 2004, 2005). While the conclusions of these investigations may be correct, the robustness of the inverted parameter values, as well as the fidelity of the gravity model as a function of wavelength, is difficult to assess. The exception is that of *Phillips* (1994) who investigated the lithospheric properties of Atla Regio, which is believed to be an active hotspot based on its geomorphology and previously determined large apparent depths of compensation. Using the loading model of *Forsyth* (1985), which assumes uncorrelated surface and subsurface loads, it was shown that a single mode of compensation could not explain the entire wavelength range of the admittance and coherence functions. An inversion utilizing only the short wavelengths yielded a crustal thickness of 30±13 km and an elastic thickness of 45±3 km. While surface loading by the volcanic constructs in this area dominates, about 10% of the load is required to be located at shallow depths within the crust. For the long-wavelength range, only the depth of the subsurface load was well constrained with a value near 150 km, and the elastic thickness was constrained only to be less than 140 km.

Finally, by using the obtained elastic thicknesses, or by forward modeling of inelastic flexure, it is possible to place constraints on the crustal temperature gradient at the time of loading. The basic approach is to match the bending moment implied by the elastic model to that predicted by an inelastic rheology (*McNutt* 1984). While the obtained temperature gradient estimates lie in the rather broad range of 3–26 K km^{-1} (*Sandwell and Schubert* 1992; *Johnson and Sandwell* 1994; *Phillips* 1994; *Brown and Grimm* 1996; *Phillips et al.* 1997), the majority of these lie on the low end, between ∼4 and 10 K km^{-1}. This is considerably lower than the expected Earth-scaled temperature gradient of ∼15 K km^{-1} (e.g., *Phillips* 1994), especially when considering that some of these estimates were obtained where an underlying mantle plume might be expected. While such calculations are critically dependent on the validity of the inelastic strength model, the assumed strain rate, and the depth dependence of temperature, these results seem to imply that the background heat flow of Venus is much less than would be expected by analogy to the Earth. Such an interpretation is consistent with a model in which the Venusian lithosphere formed catastrophically ∼500–1000 My, and has since been conductively cooling (cf. *Parmetier and Hess* 1992; *Turcotte* 1995; *Moresi and Solomatov* 1998). However, such a model

is not required, or even preferred, by the cratering history of the Venusian plains (*Hauck et al.* 1998).

8.3 Mars

Following the acquisition of high resolution gravity and topography data from the Mars Global Survey and Mars Odyssey missions, a number of studies have been published bearing on the crustal and lithospheric structure of Mars. These investigations have placed constraints on the thickness of the Martian crust, the crustal density, and the elastic thickness, and also imply the existence of dynamic support of topography and buried mass anomalies. Reviews concerning the gravity, topography and crust of Mars can be found in *Esposito et al.* (1992), *Banerdt et al.* (1992), *Zuber* (2001), *Wieczorek and Zuber* (2004), and *Nimmo and Tanaka* (2005).

The average thickness of the Martian crust has been constrained by the analysis of geoid/topography ratios over the ancient southern highlands. After removing the long-wavelength flexural and load signatures associated with the Tharsis province, a zero-elevation thickness of 57 ± 24 km was obtained under the assumption of Airy isostasy (*Wieczorek and Zuber* 2004). This range of values is consistent with estimates based upon the viscous relaxation of topography (*Nimmo and Stevenson* 2001; *Zuber et al.* 2000a) and geochemical mass-balance arguements, both of which require the crust to be less than ~ 100 km thick (see *Wieczorek and Zuber* 2004). Crustal thickness modeling further requires the mean thickness of the crust to be greater than 32 km.

A global model of the crustal thickness of Mars has been constructed by *Neumann et al.* (2004) by assuming a mean thickness of 45 km (see Figure 10). If their assumption of a constant density crust is correct, the crust of the southern highlands is predicted to be thicker by about 30 km than the northern lowlands. However, if the northern lowland crust is denser than the southern highlands, as implied by the results of *Belleguic et al.* (2005), then the actual crustal thickness difference could be significantly less. The Tharsis province is seen to possess a relatively thick crust, indicative of prolonged volcanic construction, whereas the crust beneath the major impact basins is considerably thinned, and in some places nearly absent.

Localized spectral admittance and correlation spectra have been modeled in spherical coordinates for various regions using the techniques of *Simons et al.* (1997) and *Wieczorek and Simons* (2005). In the investigations of *McGovern et al.* (2002, 2004) and *Belleguic et al.* (2005), a thin elastic spherical shell loading model was employed that depended upon the shell's elastic thickness, the load density, the crustal density, and the ratio of the magnitudes of subsurface and surface loads, which were assumed to be in or out of phase by $0°$ or $180°$. When the load density differs from that of the crust, the methodology of *Belleguic et al.* (2005) is superior, and their results are here summarized.

Of all the parameters considered by *Belleguic et al.* (2005), the load density of the major Martian volcanoes was found to be the best constrained with a value of $\sim 3200 \pm 100$ kg m^{-3}. This range is consistent with density estimates of the Martian meteorites, which are thought to be derived from these regions based on their young ages, after the inclusion

of a few percent porosity. Elastic thickness estimates are somewhat variable, but were found to lie between about 50 and 100 km when only surface loads were considered. However, when both surface and subsurface loads were modeled, only upper and lower bounds could be specified for most regions. The crustal density was constrained only beneath the Elysium rise (which is located in the northern lowlands), and was found to be identical to the density of the superposed load. Based on rock compositions at the Mars Pathfinder site, *Neumann et al.* (2004) have suggested that the southern highland crust could possess a density close to 3000 kg m^{-3}. If this inference is correct, and if the crustal density beneath the Elysium rise is representative of the northern lowlands, then this implies a hemispheric dichotomy in crustal composition. Furthermore, the low elevations of the northern plains could be a (partial) result of Pratt compensation. Finally, this study found that the inclusion of less dense subsurface loads (either compositional or thermal in origin) improved the misfit between the modeled and observed admittance functions.

Elastic thickness estimates for other locales have been determined using a variety of techniques, but these generally contain a larger number of assumptions. Modeling of the geologically inferred flexural moat of the northern polar cap suggests an elastic thickness between 60 and 120 km (*Johnson et al.* 2000). If the topography of the dichotomy boundary is flexural in origin, with loading in the northern plains, then elastic thicknesses of ~ 31–36 km are implied (*Watters* 2003). Modeling of 1-D Cartesian admittance functions have been performed by *McKenzie et al.* (2002) and *Nimmo* (2002), but the validity of the loading model was not tested by calculating theoretical correlation functions. The gravity and topography of the major Martian volcanoes were also modeled in the space domain by *Arkani-Hamed* (2000), but the finite-amplitude corrections of the modeled gravity field were not included.

One distinctive feature of Mars is the large geoid and topography signals associated with the Tharsis province (e.g., *Phillips et al.* 2001). Two possible end-member explanations for this observation are that it is either a result of voluminous extrusive lavas that are partially supported by the lithosphere, or dynamic topography associated with an underlying plume. Visco-elastic modeling of the geoid and topography response to internal buoyant loads implies that a plume is incapable of producing the totality of the observed signals (*Zhong* 2002; *Roberts and Zhong* 2004). By modeling the contributions of both surface and plume signals with a method that approximates a visco-elastic response, the degree 2 and 3 geoid/topography ratios imply that a plume can only account for ~ 15 and 25% of the geoid and topography signals, respectively. Using a modified approach that includes all spherical harmonic degrees, *Lowry and Zhong* (2003) inverted for the relative contributions of surface and internal loads and found that a plume could only account for a maximum of ~ 25 and 50% of the observed geoid and topography, respectively.

Finally, it is noted that buried mass anomalies can be investigated by examination of the residual gravity field after subtraction of an appropriate reference model. For instance, by modeling the gravity field of the Syrtis Major region by surface loading of an elastic shell, an unmodeled localized density anomaly was found beneath this volcanic province. The amplitude of this unmodeled anomaly is consistent with

the presence of dense cumulates of an extinct magma chamber (*Kiefer* 2004). Using a similar technique, buried mass anomalies have also been inferred along portions of the dichotomy boundary (*Kiefer* 2005).

8.4 The Moon

The Clementine and Lunar Prospector missions have significantly improved our knowledge of the Moon's gravity and topography. Unfortunately, the resolution of the gravity field varies dramatically between the near and farside hemispheres, and the topography derived from the Clementine altimeter is the poorest among the Earth, Venus and Mars. Indeed, the resolution of the nearside gravity field exceeds that of the topography model. Most investigations have concentrated on mapping crustal thickness variations and quantifying the attributes of the nearside impact basins and craters. A comprehensive review can be found in *Wieczorek et al.* (2006).

The thickness of the lunar crust has been estimated by the analysis of geoid/topography ratios over the nearside highland crust (*Wieczorek and Phillips* 1997). Assuming that these regions are Airy compensated, updated results presented by *Wieczorek et al.* (2006) imply an average crustal thickness of 49±16 km. The crustal structure has also been locally constrained by seismic means, primarily beneath the Apollo 12 and 14 stations (see also *Chenet et al.* 2006), but these investigations are not entirely in agreement. Initially, a value of about 60 km was reported by *Toksöz et al.* (1974), but more recent studies imply thinner values of 45±5 km (*Khan et al.* 2000), 38±8 (*Khan and Mosegaard* 2002), and 30±2.5 km (*Lognonné et al.* 2003). When the elevations of the Apollo stations are taken into account, the measured geoid/topography ratios are most consistent with the recent thin-crust seismic estimates.

By assuming values for the mean crustal thickness, as well as the density of the crust and mantle, it is possible to construct a global crustal thickness model of the Moon (see *Wieczorek and Phillips* 1998; *Wieczorek et al.* 2006, and section 5). The most notable feature of these models is the dramatic thinning of the crust beneath the large impact basins. This is a natural consequence of the large quantity of material that is ballistically excavated during the impact process (e.g., *Wieczorek and Phillips* 1999), and it is seen that the depth of excavation reaches several tens of kilometers beneath the largest basins. It seems probable that some basins, such as Crisium, might even have excavated into the underlying mantle given their inferred near-zero crustal thicknesses. Nevertheless, despite the great size of the giant South Pole-Aitken basin on the farside, it appears that its depth of excavation was relatively shallow, and that ∼20 km of crustal materials are present there. If the assumption of a constant density crust is correct, then the ∼1.9 km center-of-mass/center-of-figure offset implies that the farside crust is thicker than the nearside hemisphere by about 15 km. However, global scale variations in crustal composition are known to exist (see *Jolliff et al.* 2000), and if these affect the crustal density, the hemispheric difference in crustal thickness could be much less.

The largest lunar impact basins (excluding the South Pole-Aitken basin) are characterized by having low elevations and large positive gravity anomalies, a signature generally referred to as a *mascon* basin. The positive gravitational anomalies are likely a result of both uplift of the underlying crust-mantle interface, and the flexural support of surface mare basalt flows. Based on estimates of the mare basalt thicknesses, which can reach a few kilometers within the central portions of some impact basins, it appears that the crust-mantle interface has, in some cases, been uplifted above its pre-mare isostatic position (e.g., *Neumann et al.* 1996; *Wieczorek and Phillips* 1999). This hypothesis is supported by the existence of mascon basins that lack evidence of mare volcanism (*Konopliv et al.* 1998). Those basins that are in a pre-mare isostatic state appear to be confined to a region of the crust that is enhanced in heat producing elements, and which likely possesses higher temperatures (*Wieczorek and Phillips* 1999, 2000). In contrast to the largest impact basins, intermediate-sized craters have negative gravity anomalies and generally show some form of compensation (e.g., *Reindler and Arkani-Hamed* 2001). Only about 15% of the craters in the *Reindler and Arkani-Hamed* (2001) study appear to be completely uncompensated, or to possess excess negative gravity anomalies due to crustal brecciation. For these intermediate sized craters, there does not appear to be any correlation of compensation state with crater age or location.

A few studies have attempted to place constrains on the elastic thickness of the Moon using both gravity and topography data (e.g., *Arkani-Hamed* 1998; *Crosby and McKenzie* 2005; *Sugano and Heki* 2004). Most analyses have concentrated on the mascon basins, but unfortunately, the validity of the employed assumptions is often difficult to quantify. A proper analysis requires an assessment of (1) whether or not the mascon basins were in an isostatic (or super-isostatic) state before they were loaded by mare basalts, (2) the geometry and thickness of the mare basalt loads, (3) finite amplitude contributions of the uplifted crust-mantle interface, (4) both the admittance and correlation functions if the analysis is performed in the spectral domain, (5) a loading model that takes account of the surface and subsurface loads and their unknown phase relationship, and (6) the proper diameter of a basin ("main topographic rims" often differ significantly from the more relevant diameter of the excavation cavity (*Wieczorek and Phillips* 1999)). An alternative method for estimating the elastic thickness is by comparing the location of tectonic features (such as faults and graben) to that predicted by a specified loading model (e.g., *Solomon and Head* 1980). Detailed modeling of the Serenitatis basin (*Freed et al.* 2001) suggests that its elastic thickness was about 25 km when the concentric rilles formed, and probably greater than 70 km when the younger compressional ridges formed.

Finally, one curious large-scale feature of Moon is the amplitude of its degree-2 gravity and topography terms. If the Moon were in hydrostatic equilibrium, then the amplitude of the C_{20} and C_{22} terms would be directly relatable to the Earth-Moon separation (cf. eq. 18). The present day magnitudes of these coefficients, however, are much greater than would be expected for equilibrium at the present time. This has led to the suggestion that the equilibrium shape of the Moon was frozen into the lithosphere when it was closer to the Earth early in its orbital evolution (e.g., *Jeffreys* 1976). If the observed magnitudes are interpreted as a relict equilibrium shape, then the corresponding Earth-Moon separa-

tion is about 25 Earth radii (the current separation is about 60 Earth radii) (*Lambeck and Pullan* 1980). This interpretation is somewhat problematical as the lunar orbit is predicted to have receded beyond this distance in less than ∼100 My after the formation of the Earth-Moon system (e.g., *Webb* 1982). Alternatively, it is possible that this shape is a result of large-scale crustal thickness variations, or lateral variations in mantle density.

9   FUTURE DEVELOPMENTS AND CONCLUDING REMARKS

The gravitational fields and topography of the terrestrial planets have become increasingly better characterized since the discovery of lunar "mascons" by Muller and Sjogren in 1968. While the early data sets were quite sparse, the gradual accumulation of data with each successive space mission have given rise to near-global gravity and topography spherical harmonic models. Some of the gravity models now possess spherical harmonic bandwidths greater than 100, and future missions will surely lead to vast improvements. With the exception of the Moon, the topography has been measured to an accuracy that exceeds that of the corresponding gravity model.

Not only has the resolution of the planetary data sets continued to improve with time, but so have the analysis techniques. Early investigations were often restricted to analyses of individual 1-D line-of-sight gravitational acceleration profiles. As data coverage became more dense, 2-D regional models were developed that were more often than not analyzed using Cartesian techniques developed for the Earth. Because of the small size of some planetary bodies, such as the Moon, the assumption of Cartesian geometry has been called into question, and spherical analysis methods have proven to be superior. In the past ten years, the full suite of Cartesian gravity-topography analysis techniques have been developed for the sphere, including multitaper spectral analysis, the rapid calculation of gravitational anomalies from finite amplitude topographic relief, and realistic admittance models that take into account surface and subsurface loading with an arbitrary phase relationship. Though the approximation of Cartesian geometry may not incur large errors for some small-scale investigations, it is currently just as easy to use a spherical-based method that possess a comparable computational speed.

While much has been learned about the crustal and lithospheric structure of the terrestrial planets, there is still much to be done. In particular, in hindsight it is now clear that many gravity-topography admittance and coherence studies have used analysis techniques that can yield unreliable results. Shortcomings include incorrect application of the multitaper spectral analysis technique, the neglect of either the admittance or correlation function, and the use of a theoretical admittance model that might be an oversimplification of reality. Few studies, even for the Earth, have performed these analyses entirely correctly, and one should be quite skeptical of the majority of elastic thickness estimates that have been published for regions where subsurface loading is important.

It is also important to note that the concept of an "elastic" lithosphere is in actuality a gross oversimplification of reality. Because of the ease of generating a time-invariant flexural profile from a load emplaced on an elastic plate, we would like to hope that the obtained "effective elastic thickness" has some meaning. While this might be true for regions where the magnitude of surface and subsurface loading is small, and where inplane forces are absent, it has been demonstrated that the use of a more realistic rheology can yield flexural profiles that sometimes are quite different. Unfortunately, the most realistic elastoviscoplastic models are computationally expensive, and are not currently amenable to a robust inversion procedure using gravity and topography as constraints. Though a simpler elastic-plastic formulation could be used in such an inversion, this rheological model utilizes assumptions that still might be too simplistic. Nevertheless, it would be appropriate to develop an elastic-plastic loading model similar to the elastic model described in section 7. One benefit of such a model is that it would be possible to invert for the regional heat flow. An additional avenue of future research is to compare the locations of surface faulting with those predicted from elastic, elastic-plastic, and elastoviscoplastic models.

Finally, it is worth mentioning that significant improvements will be made to our knowledge of the gravitational fields and topography of the terrestrial planets. In particular, while the land-based topography for the Earth is now known to high accuracy, there are still gaps near the polar regions that could be partially filled by data obtained by the orbiting GLAS laser altimeter (e.g., *Abshire et al.* 2005; *Schutz et al.* 2005; *Shuman et al.* 2006). The soon to be launched satellite GOCE, which contains a gravity gradiometer, will lead to improved models of the terrestrial gravity field. An area of active research for the Earth, but also for the other planets in a more limited sense, is that of measuring and modeling time variable gravity signatures that are a result of hydrologic processes and tidal deformation.

In addition to the Earth, spacecraft missions to the other terrestrial planets are bound to yield surprises. The lunar topography will be dramatically improved by the upcoming SELENE and Lunar Reconnaissance Orbiter (LRO) missions. Analysis of data obtained from the SELENE relay satellite, as well as dense altimetric cross-overs from LRO, will furthermore vastly improve our knowledge of the Moon's farside gravity field. The gravity field of Mars will be improved by data obtained from the currently orbiting Mars Reconnaissance Orbiter. The topography and gravity field of Mercury will be characterized globally for the first time from the MESSENGER and BepiColumbo missions. In addition, missions are currently being proposed to measure the gravity and topography of bodies in the outer solar system, such as the satellites of Jupiter and Saturn.

REFERENCES

Abshire, J. B., X. Sun, H. Riris, J. M. Sirota, J. F. McGarry, S. Palm, D. Yi, and P. Liiva, Geoscience Laser Altimeter System (GLAS) on the ICESat mission: On-orbit measurement performance, *Geophys. Res. Lett.*, *32*, L21S02, doi:10.1029/2005GL024,028, 2005.

Albert, R., and R. J. Phillips, Paleoflexure, *Geophys. Res. Lett.*, *27*, 2385–2388, 2000.

Albert, R., R. J. Phillips, A. Dombard, and C. Brown, A test of the validity of yield strength envelopes with an elastoviscoplastic finite element model, *Geophys. J. Int.*, *140*, 399–409, 2000.

Anderson, J. D., G. Colombo, P. B. Esposito, E. L. Lau, and G. B. Trager, The mass, gravity field, and ephemeris of Mercury, *Icarus*, *71*, 337–349, 1987.

Anderson, J. D., R. F. Jurgens, E. L. Lau, M. A. S. III, and G. Schubert, Shape and orientation of Mercury from radar ranging data, *Icarus*, *124*, 690–697, 1996a.

Anderson, J. D., E. L. Lau, W. L. Sjogren, G. Schubert, and W. B. Moore, Gravitational constraints on the internal structure of ganymede, *Nature*, *384*, 541–543, 1996b.

Anderson, J. D., W. L. Sjogren, and G. Schubert, Galileo gravity results and the internal structure of Io, *Science*, *272*, 709–712, 1996c.

Anderson, J. D., G. Schubert, R. A. Jacobson, E. L. Lau, W. B. Moore, and W. L. Sjogren, Europa's differentiated internal structure: Inferences from four galileo encounters, *Science*, *281*, 2019–2022, 1998.

Anderson, J. D., R. A. Jacobson, E. L. Lau, W. B. Moore, and G. Schubert, Io's gravity field and interior structure, *J. Geophys. Res.*, *106*, 32,963–32,969, 2001a.

Anderson, J. D., R. A. Jacobson, T. P. McElrath, W. B. Moore, and G. Schubert, Shape, mean radius, gravity field, and interior structure of Callisto, *Icarus*, *153*, 157–161, 2001b.

André, S. L., T. R. Watters, and M. S. Robinson, The long wavelength topography of Beethoven and Tolstoj basins, Mercury, *Geophys. Res. Lett.*, *32*, L21,202, doi:10.1029/2005GL023,627, 2005.

Arkani-Hamed, J., The lunar mascons revisited, *J. Geophys. Res.*, *103*, 3709–3739, 1998.

Arkani-Hamed, J., Strength of Martian lithosphere beneath large volcanoes, *J. Geophys. Res.*, *105*, 26,713–26,732, 2000.

Balmino, G., The spectra of the topography of the Earth, Venus and Mars, *Geophys. Res. Lett.*, *20*(11), 1063–1066, 1993.

Balmino, G., Gravitational potential harmonics from the shape of an homogeneous body, *Celest. Mech. Dyn. Astron.*, *60*, 331–364, 1994.

Banerdt, W. B., Support of long-wavelength loads on Venus and implications for internal structure, *J. Geophys. Res.*, *91*, 403–419, 1986.

Banerdt, W. B., M. Golombek, and K. Tanaka, Stress and tectonics on Mars, in *Mars*, edited by H. Kieffer, B. Jakosky, C. Snyder, and M. Matthews, pp. 249–297, Univ. of Arizona Press, Tucson, 1992.

Banks, R. J., S. C. Francis, and R. G. Hipkin, Effects of loads in the upper crust on estimates of the elastic thickness of the lithosphere, *Geophys. J. Int.*, *145*, 291–299, 2001.

Barnett, D. N., F. Nimmo, and D. McKenzie, Elastic thickness estimates for Venus using line of sight accelerations from Magellan cycle 5, *Icarus*, *146*, 404–419, 2000.

Barnett, D. N., F. Nimmo, and D. McKenzie, Flexure of Venusian lithosphere measured from residual topography and gravity, *J. Geophys. Res.*, *107*, E2, doi:10.1029/2000JE001,398, 2002.

Bechtel, T. D., D. W. Forsyth, and C. J. Swain, Mechanisms of isostatic compensation in the vicinity of the East African Rift, Kenya, *Geophys. J. R. Astron. Soc.*, *90*, 445–465, 1987.

Bechtel, T. D., D. W. Forsyth, V. L. Sharpton, and R. A. F. Grieve, Variations in effective elastic thickness of the North-American lithosphere, *Nature*, *343*(6259), 636–638, 1990.

Belleguic, V., P. Lognonné, and M. Wieczorek, Constraints on the Martian lithosphere from gravity and topography data, *J. Geophys. Res.*, *110*, E11,005, doi:10.1029/2005JE002,437, 2005.

Bills, B. G., and F. G. Lemoine, Gravitational and topographic isotropy of the Earth, Moon, Mars, and Venus, *J. Geophys. Res.*, *100*, 26,275–26,295, 1995.

Blakely, R. J., *Potential Theory in Gravity and Magnetic Applications*, Cambridge Univ. Press, New York, 1995.

Brown, C. D., and R. E. Grimm, Lithospheric rheology and flexure at Artemis Chasma, Venus, *J. Geophys. Res.*, *101*(E5), 12,697–12,708, 1996.

Brown, C. D., and R. J. Phillips, Crust-mantle decoupling by flexure of continental lithosphere, *J. Geophys. Res.*, *105*(B6), 13,221–13,237, 2000.

Burov, E. B., and M. Diament, The effective elastic thickness (T_e) of continental lithosphere: What does it really mean?, *J. Geophys. Res.*, *100*(B3), 3905–3927, 1995.

Ceuleneer, G., M. Rabinowicz, M. Monnereau, A. Cazenave, and C. Rosemberg, Viscosity and thickness of the sub-lithospheric low-viscosity zone: constraints from geoid and depth over oceanic swells, *Earth Planet. Sci. Lett.*, *89*, 84–102, 1988.

Chambat, F., and B. Valette, Earth gravity up to second order in topography and density, *Phys. Earth Planet. Inter.*, *151*, 89–106, 2005.

Chao, B. F., and D. P. Rubincam, The gravitational field of Phobos, *Geophys. Res. Lett.*, *16*, 859–862, 1989.

Chenet, H., P. Lognonné, M. Wieczorek, and H. Mizutani, Lateral variations of lunar crustal thickness from the Apollo seismic data set, *Earth Planet. Sci. Lett.*, *243*, 1–14, 2006.

Cheng, A. F., et al., Small-scale topography of 433 Eros from laser altimetry and imaging, *Icarus*, *155*, 51–74, 2002.

Cook, A. C., T. R. Watters, M. S. Robinson, P. D. Spudis, and D. B. J. Bussey, Lunar polar topography derived from clementine stereoimages, *J. Geophys. Res.*, *105*, 12,023–12,033, 2000.

Crosby, A., and D. McKenzie, Measurements of the elastic thickness under ancient lunar terrain, *Icarus*, *173*, 100–107, 2005.

Dahlen, F. A., and J. Tromp, *Theoretical Global Seismology*, Princeton Univ. Press, Princeton, N. J., 1998.

Dermott, S. F., Shapes and gravitational moments of satelites and asteroids, *Icarus*, *37*, 575–586, 1979.

Dorman, L. M., and B. T. Lewis, Experimental isostasy, 1, Theory of the determination of the Earth's isostatic response to a concentrated load, *J. Geophys. Res.*, *75*(17), 3357–3365, 1970.

Driscoll, J. R., and D. M. Healy, Computing Fourier transforms and convolutions on the 2-sphere, *Adv. Appl. Math.*, *15*, 202–250, 1994.

Duxbury, T. C., The figure of Phobos, *Icarus*, *78*, 169–180, 1989.

Ebinger, C., T. Bechtel, D. Forsyth, and C. Bowin, Effective elastic plate thickness beneath the east African and Afar plateaus and dynamic compensation of the uplifts, *J. Geophys. Res.*, *94*(B3), 2883–2901, 1989.

Esposito, P., W. Benerdt, G. Lindal, W. Sjogren, and M. Slade, Gravity and topography, in *Mars*, edited by H. Kieffer, B. Jakosky, C. Snyder, and M. Matthews, pp. 209–248, Univ. of Arizona Press, Tucson, 1992.

Fedi, M., and G. Florio, A stable downward continuation by using the ISVD method, *Geophys. J. Int.*, *151*, 146–156, 2002.

Ford, P., and G. Pettengill, Venus topography and kilometer-scale slopes, *J. Geophys. Res.*, *97*, 13,103–13,114, 1992.

Forsyth, D. W., Subsurface loading and estimates of the flexural rigidity of continental lithosphere, *J. Geophys. Res.*, *90*(B14), 12,623–12,632, 1985.

Freed, A. M., H. J. Melosh, and S. C. Solomon, Tectonics of mascon loading: Resolution of the strike-slip faulting paradox, *J. Geophys. Res.*, *106*, 20,603–20,620, 2001.

Garmier, R., and J.-P. Barriot, Ellipsoidal harmonic expansions of the gravitational potential: Theory and application, *Celest. Mech. Dynam. Astron.*, *79*, 235–275, 2001.

Garmier, R., and J.-P. Barriot, Modeling of the Eros gravity field as an ellipsoidal harmonic expansion from the NEAR doppler tracking data, *Geophys. Res. Lett.*, *29*, doi:10.1029/2001GL013,768, 2002.

Ghent, E. D., G. M. Dipple, and J. K. Russell, Thermodynamic models for eclogite mantle lithosphere, *J. Geophys. Res.*, *218*, 451–462, 2004.

Giese, B., J. Oberst, T. Roatsch, G. Neukum, J. W. Head, and R. Pappalardo, The local topography of Uruk Sulcus and Galileo Regio obtained from stereo images, *Icarus*, *135*, 303–316, 1998.

Goossens, S., P. N. A. M. Visser, and B. A. C. Ambrosius, A method to determine regional lunar gravity fields from earth-based satellite tracking

data, *Planet. Space Sci.*, *53*, 1331–1340, 2005.

Goossens, S., P. N. A. M. Visser, K. Heki, and B. A. C. Ambrosius, Local gravity from Lunar Prospector tracking data: results of Mare Serenitatis, *Earth Planets Space*, in press.

Grimm, R. E., The deep structure of Venusian plateau highlands, *Icarus*, *112*, 89–103, 1994.

Grimm, R. E., and P. C. Hess, The crust of Venus, in *Venus II*, edited by S. W. Bougher, D. M. Hunten, and R. J. Phillips, pp. 1205–1244, Univ. of Arizona Press, Tucson, 1997.

Grimm, R. E., and R. J. Phillips, Gravity anomalies, compensation mechanisms, and the geodynamics of Western Ishtar Terra, Venus, *J. Geophys. Res.*, *96*(B6), 8309–8324, 1991.

Haines, G. V., Spherical cap harmonic analysis, *J. Geophys. Res.*, *90*, 2583–2591, 1985.

Hansen, V. L., and R. J. Phillips, Formation of Ishtar Terra, Venus: surface and gravity constraints, *Geology*, *23*, 292–296, 1995.

Harmon, J. K., D. B. Campbell, D. L. Bindschadler, J. W. Head, and I. I. Shapiro, Radar altimetry of Mercury: A preliminary analysis, *J. Geophys. Res.*, *91*, 385–401, 1986.

Hastings, D. A., and P. K. Dunbar, *Global Land One-kilometer Base Elevation (GLOBE) Digital Elevation Model, Documentation, Volume 1.0. Key to Geophysical Records Documentation (KGRD) 34*, National Oceanic and Atmospheric Administration, National Geophysical Data Center, 325 Broadway, Boulder, Colorado, 80303, USA, 1999.

Hauck, S. A., III, R. J. Phillips, and M. H. Price, Venus: Crater distribution and plains resurfacing models, *J. Geophys. Res.*, *103*(E6), 13,635–13,642, 1998.

Haxby, W. F., and D. L. Turcotte, On isostatic geoid anomalies, *J. Geophys. Res.*, *83*, 5473–5478, 1978.

Heiskanen, W. A., and H. Moritz, *Physical Geodesy*, Freeman, San Francisco, Calif., 1967.

Holmes, S. A., and W. E. Featherstone, A unified approach to the Clenshaw summation and the recursive computation of very high degree and order normalised associated Legendre functions, *J. Geodesy*, *76*, 279–299, 2002.

Hoogenboom, T., S. E. Smrekar, F. S. Anderson, and G. Houseman, Admittance survey of type 1 coronae on Venus, *J. Geophys. Res.*, *109*, E03,002, doi:10.1029/2003JE002,171, 2004.

Hoogenboom, T., T. G. Houseman, and P. Martin, Elastic thickness estimates for coronae associated with chasmata on Venus, *J. Geophys. Res.*, *110*, E09,003, doi:10.1029/2004JE002,394, 2005.

Hwang, C., and S.-K. Chen, Fully normalized spherical cap harmonics: Application to the analysis of sea-level data from TOPEX/POSEIDON and ERS-1, *Geophys. J. Int.*, *129*, 450–460, 1997.

Hwang, C., and B. Parsons, An optimal procedure for determining gravity from multi-satellite altimetry, *Geophys. J. Int.*, *125*, 705–719, 1996.

Jeffreys, H., *The Earth: its origin history and physical constitution*, 6th ed., 586 pp., Cambridge University Press, 1976.

Johnson, C., S. Solomon, J. W. H. III, R. J. Phillips, D. Smith, and M. Zuber, Lithospheric loading by the northern polar cap on Mars, *Icarus*, *144*, 313–328, 2000.

Johnson, C. L., and D. T. Sandwell, Lithospheric flexure on Venus, *Geophys. J. Int.*, *119*, 627–647, 1994.

Jolliff, B. J., J. J. Gillis, L. A. Haskin, R. L. Korotev, and M. A. Wieczorek, Major lunar crustal terranes: Surface expressions and crust-mantle origins, *J. Geophys. Res.*, *105*, 4197–4216, 2000.

Kaula, W. M., Theory of statistical analysis of data distributed over a sphere, *Rev. Geophys.*, *5*(1), 83–107, 1967.

Kaula, W. M., *Theory of satellite geodesy: Applications of satellites to geodesy*, Dover, Mineola, NY, 2000.

Khan, A., and K. Mosegaard, An enquiry into the lunar interior–a non-linear inversion of the apollo lunar seismic data, *J. Geophys. Res.*, *107*(E6), 10.1029/2001JE001,658, 2002.

Khan, A., K. Mosegaard, and K. K. L. Rasmussen, A new seismic velocity model for the moon from a monte carlo inversion of the apollo lunar seismic data, *Geophys. Res. Lett.*, *27*, 1591–1594, 2000.

Kiefer, W., Gravity evidence for an extinct magma chamber beneath Syrtis Major, Mars: a look at the magmatic plumbing system, *Earth Planet. Sci.*

Lett., *222*, 349–361, 2004.

Kiefer, W., Buried mass anomalies along the hemispheric dichotomy in eastern Mars: Implications for the origin and evolution of the dichotomy, *Geophys. Res. Lett.*, *32*, L22,201, doi:10.1029/2005GL024,260, 2005.

Kiefer, W. S., and B. F. Hager, A mantle plume model for the equatorial highlands of Venus, *J. Geophys. Res.*, *96*(E4), 20,947–20,966, 1991.

Kiefer, W. S., M. A. Richards, and B. H. Hager, A dynamic model of Venus's gravity field, *Geophys. Res. Lett.*, *13*(1), 14–17, 1986.

Konopliv, A. S., A. B. Binder, L. L. Hood, A. B. Kucinskas, W. L. Sjogren, and J. G. Williams, Improved gravity field of the Moon from Lunar Prospector, *Science*, *281*, 1476–1480, 1998.

Konopliv, A. S., W. B. Banerdt, and W. L. Sjogren, Venus gravity: 180th degree and order model, *Icarus*, *139*, 3–18, 1999.

Konopliv, A. S., S. W. Asmar, and D. N. Yuan, Recent gravity models as a result of the Lunar Prospector mission, *Icarus*, *150*, 1–18, 2001.

Konopliv, A. S., C. F. Yoder, E. M. Standish, D.-N. Yuan, and W. L. Sjogren, A global solution for the Mars static and seasonal gravity, Mars orientation, Phobos and Deimos masses, and Mars ephemeris, *Icarus*, *182*, 23–50, 2006.

Kraus, H., *Thin elastic shells: An introduction to the theoretical foundations and the analysis of their static and dynamic behavior*, 467 pp., John Wiley, New York, 1967.

Kucinskas, A. B., and D. T. Turcotte, Isostatic compensation of equatorial highlands on Venus, *Icarus*, *112*, 104–116, 1994.

Lambeck, K., *Geophysical Geodesy*, Oxford Univ. Press, New York, 1988.

Lambeck, K., and S. Pullan, The lunar fossil bulge hypothesis revisited, *Phys. Earth Planet. Inter.*, *22*, 29–35, 1980.

Lawrence, K. P., and R. J. Phillips, Gravity/topography admittance inversion on Venus using niching genetic algorithms, *Geophys. Res. Lett.*, *30*(19), 1994, doi:10.1029/2003GL017,515, 2003.

Lemoine, F., et al., *The Development of the Joint NASA GSFC and the National Imagery and Mapping Agency (NIMA) Geopotential Model EGM96*, NASA Goddard Space Flight Cent., Greenbelt, Md., 1998.

Lemoine, F. G., D. E. Smith, D. D. Rowlands, M. T. Zuber, G. A. Neumann, D. S. Chinn, and D. E. Pavlis, An improved solution of the gravity field of Mars (GMM-2B) from Mars Global Surveyor, *J. Geophys. Res.*, *106*(E10), 23,359–23,376, 2001.

Lognonné, P., J. Gagnepain-Beyneix, and H. Chenet, A new seismic model for the moon: Implications for structure, thermal evolution and formation of the Moon, *Earth Planet. Sci. Lett.*, *211*, 27–44, 2003.

Lowry, A. R., and S. Zhong, Surface versus internal loading of the Tharsis rise, Mars, *J. Geophys. Res.*, *E9*, 5099, doi:10.1029/2003JE002,111, 2003.

Margot, J.-L., D. B. Campbell, R. F. Jurgens, and M. A. Slade, Topography of tycho crater, *J. Geophys. Res.*, *104*, 11,875–811,882, 1999a.

Margot, J.-L., D. B. Campbell, R. F. Jurgens, and M. A. Slade, Topography of the lunar poles from radar interferometry: A survey of cold trap locations, *Science*, *284*, 1658–1660, 1999b.

Marks, K. M., and W. H. F. Smith, An evaluation of publicly available global bathymetry grids, *Marine Geophys. Res.*, *27*, 19–34, 2006.

Martinec, Z., K. Pěč, and M. Burša, The Phobos gravitational field modeled on the basis of its topography, *Earth Moon Planets*, *45*, 219–235, 1989.

McGovern, P. J., et al., Localized gravity/topography admittance and correlation spectra on Mars: Implications for regional and global evolution, *J. Geophys. Res.*, *107*(E12), 5136, doi:10.1029/2002JE001,854, 2002.

McGovern, P. J., et al., Correction to "Localized gravity/topography admittance and correlation spectra on Mars: Implications for regional and global evolution", *J. Geophys. Res.*, *109*(E07007), doi:10.1029/2004JE002,286, 2004.

McKenzie, D., The relationship between topography and gravity on Earth and Venus, *Icarus*, *112*, 55–88, 1994.

McKenzie, D., Estimating t_e in the presence of internal loads, *J. Geophys. Res.*, *108*(B9), 2348, doi: 10.1029/2002JB001,766, 2003.

McKenzie, D., and F. Nimmo, Elastic thickness estimates for Venus from line of sight accelerations, *Icarus*, *130*, 198–216, 1997.

McKenzie, D. P., D. N. Barnett, and D.-N. Yuan, The relationship between Martian gravity and topography, *Earth Planet. Sci. Lett.*, *195*, 1–

16, 2002.

McNutt, M. K., Lithospheric flexure and thermal anomalies, *J. Geophys. Res.*, *89*(B13), 11,180–11,194, 1984.

Miller, J. K., et al., Determination of shape, gravity, and rotational state of asteroid 433 Eros, *Icarus*, *155*, 3–17, 2002.

Mohr, P. J., and B. N. Taylor, CODATA recommended values of the fundamental physical constants: 2002, *Rev. Mod. Phys.*, *77*, 1–107, 2005.

Moore, W. B., and G. Schubert, Lithospheric thickness and mantle/lithosphere density contrast beneath Beta Regio, Venus, *Geophys. Res. Lett.*, *22*(4), 429–432, 1995.

Moore, W. B., and G. Schubert, Venusian crustal and lithospheric properties from nonlinear regressions of highland geoid and topopgraphy, *Icarus*, *128*, 415–428, 1997.

Moresi, L., and V. Solomatov, Mantle convection with a brittle lithosphere: thoughts on the global tectonic styles of the Earth and Venus, *Geophys. J. Int.*, *133*, 669–682, 1998.

Mueller, S., and R. J. Phillips, On the reliability of lithospheric constraints derived from models of outer-rise flexure, *Geophys. J. Int.*, *123*, 887–902, 1995.

Muller, P. M., and W. L. Sjogren, Masons: lunar mass concentrations, *Science*, *161*, 680–684, 1968.

National Geophysical Data Center, *ETOPO2 global 2′ elevations [CD-ROM]*, U.S. Department of Commerce, National Oceanic and Atmospheric Administration, Boulder, Colorado, USA, 2001.

National Imagery and Mapping Agency, *Department of Defense World Geodetic System 1984: its definition and relationship with local geodetic systems*, NIMA TR8350.2, 175 pp., National Imagery and Mapping Agency, 2000.

Neumann, G. A., M. T. Zuber, D. E. Smith, and F. G. Lemoine, The lunar crust: Global structure and signature of major basins, *J. Geophys. Res.*, *101*, 16,841–16,843, 1996.

Neumann, G. A., D. D. Rowlands, F. G. Lemoine, D. E. Smith, and M. T. Zuber, Crossover analysis of Mars Orbiter Laser Altimeter data, *J. Geophys. Res.*, *106*, 23,753–23,768, 2001.

Neumann, G. A., M. T. Zuber, M. A. Wieczorek, P. J. McGovern, F. G. Lemoine, and D. E. Smith, Crustal structure of Mars from gravity and topography, *J. Geophys. Res.*, *109*(E08002), doi:10.1029/2004JE002,262, 2004.

Nimmo, F., Admittance estimates of mean crustal thickness and density at the Martian hemispheric dichotomy, *J. Geophys. Res.*, *107*(E11), 5117, doi:10.1029/2000JE001,488, 2002.

Nimmo, F., and D. McKenzie, Volcanism and tectonics on Venus, *Annu. Rev. Earth Planet. Sci.*, *26*, 23–51, 1998.

Nimmo, F., and D. J. Stevenson, Estimates of martian crustal thickness from viscous relaxation of topography, *J. Geophys. Res.*, *106*, 5085–5098, 2001.

Nimmo, F., and K. Tanaka, Earth crustal evolution of Mars, *Annu. Rev. Earth Planet. Sci.*, *33*, 133–161, doi:10.1146/annurev.earth.33.092,203.122,637, 2005.

Nimmo, F., B. Giese, and R. T. Pappalardo, Estimates of Europa's ice shell thickness from elastically-supported topography, *Geophys. Res. Lett.*, *30*, 1233, doi:10.1029/2002GL016,660, 2003a.

Nimmo, F., R. T. Pappalardo, and G. Giese, On the origins of band topography, Europa, *Icarus*, *166*, 21–32, 2003b.

Ockendon, J. R., and D. L. Turcotte, On the gravitational potential and field anomalies due to thin mass layers, *Geophys. J. R. Astron. Soc.*, *48*, 479–492, 1977.

Panasyuk, S. V., and B. H. Hager, Inversion for mantle viscosity profiles constrained by dynamic topography and the geoid, and their estimated errors, *Geophys. J. Int.*, *143*, 821–836, 2000.

Parker, R. L., The rapid calculation of potential anomalies, *Geophys. J. R. Astron. Soc.*, *31*, 447–455, 1972.

Parmetier, E. M., and P. C. Hess, Chemical differentiation of a convecting planetary interior: Consequences for a one plate planet such as Venus, *—Geophys. Res. Lett.*, *19*(20), 2015–2018, 1992.

Percival, D. B., and A. T. Walden, *Spectral Analysis for Physical Applications, Multitaper and Conventional Univariate Techniques*, Cambridge Univ. Press, New York, 1993.

Pérez-Gussinyé, M., A. Lowry, A. B. Watts, and I. Velicogna, On the recovery of effective elastic thickness using spectral methods: Examples from synthetic data and from the Fennoscandian Shield, *J. Geophys. Res.*, *109*, B10,409, doi:10.1029/2003JB002,788, 2004.

Phillips, R. J., Estimating lithospheric properties at Atla Regio, *Icarus*, *112*, 147–170, 1994.

Phillips, R. J., and K. Lambeck, Gravity fields of the terrestrial planets: Long-wavelength anomalies and tectonics, *Rev. Geophys.*, *18*(1), 27–76, 1980.

Phillips, R. J., C. L. Johnson, S. J. Mackwell, P. Morgan, D. T. Sandwell, and M. T. Zuber, Lithospheric mechanics and dynamics of Venus, in *Venus II*, edited by S. W. Bougher, D. M. Hunten, and R. J. Phillips, pp. 1163–1204, Univ. of Arizona Press, Tucson, 1997.

Phillips, R. J., et al., Ancient geodynamics and global-scale hydrology on Mars, *Science*, *291*, 2587–2591, 2001.

Phipps Morgan, J., and D. K. Blackman, Inversion of combined gravity and bathymetry data for crustal structure: A prescription for downward continuation, *Earth Planet. Sci. Lett.*, *119*, 167–179, 1993.

Press, W. H., S. A. Teukolsky, W. T. Vetterling, and B. P. Flannery, *Numerical Recipes in FORTRAN: The Art of Scientific Computing*, 2nd ed., Cambridge Univ. Press, 1992.

Rabus, P. B., M. Eineder, A. Roth, and R. Bamler, The shuttle radar topography mission—a new class of digital elevation models acquired by spaceborne radar, *Photogramm. Rem. Sens.*, *57*, 241–262, 2003.

Rapp, R. H., The decay of the spectrum of the gravitational potential and the topography of the Earth, *Geophys. J. Int.*, *99*, 449–455, 1989.

Rappaport, N. J., A. S. Konopliv, and A. B. Kucinskas, An improved 360 degree and order model of Venus topography, *Icarus*, *139*, 19–31, 1999.

Reigber, C., R. Schmidt, F. Flechtner, R. König, U. Meyer, K.-H. Neumayer, P. Schwintzer, and S. Y. Zhu, An Earth gravity field model complete to degree and order 150 from GRACE: EIGEN-GRACE02S, *J. Geodynamics*, *39*, 1–10, 2005.

Reigber, C., et al., Earth gravity field and seasonable variability from CHAMP, in *Earth observations with CHAMP*, edited by C. Reigber, H. Lühr, P. Schwintzer, and J. Wickert, pp. 25–30, Springer, Berlin, 2004.

Reindler, L., and J. Arkani-Hamed, The compensation state of intermediate size lunar craters, *Icarus*, *153*, 71–88, 2001.

Roberts, J., and S. Zhong, Plume-induced topography and geoid anomalies and their implications for the Tharsis rise on Mars, *J. Geophys. Res.*, *109*, E03,009, doi:10.1029/2003JE002,226, 2004.

Robinson, E. M., and B. Parsons, Effect of a shallow low-viscosity zone on the formation of midplate swells, *J. Geophys. Res.*, *93*(B4), 3144–3156, 1988.

Rodríguez, E., C. S. Morris, J. E. Belz, E. C. Chapin, J. M. Martin, W. Daffer, and S. Hensley, An assessment of the SRTM topographic products, *Tech. rep.*, Jet Propulsion Laboratory, 2005.

Rogers, P. G., and M. T. Zuber, Tectonic evolution of Bell Regio, Venus: Regional stress, lithospheric flexure, and edifice stresses, *J. Geophys. Res.*, *103*(E7), 16,841–16,853, 1998.

Rosenblatt, P., P. Pinet, and E. Touvenot, Comparative hypsometric analysis of Earth and Venus, *Geophys. Res. Lett.*, *21*, 465–468, 1994.

Rosiek, M. R., and R. Aeschliman, Lunar shaded relief map updated with Clementine data, *Lunar Planet. Sci.*, *XXXII (CD-ROM)*, 1943, 2001.

Rummel, R., Gravity and topography of Moon and planets, *Earth Moon Planets*, *94*, 103–111, doi:10.1007/s11,038–005–3245–z, 2005.

Sandwell, D. T., and G. Schubert, Flexural ridges, trenches, and outer rises around coronae on Venus, *J. Geophys. Res.*, *97*(E10), 16,069–16,083, 1992.

Sandwell, D. T., and W. H. F. Smith, Marine gravity anomaly from Geosat and ERS 1 satellite altimetry, *J. Geophys. Res.*, *102*(B5), 10,039–10,054, 1997.

Scheeres, D. J., B. Khushalani, and R. A. Werner, Estimating asteroid density distributions from shape and gravity information, *Planet. Space Sci.*, *48*, 965–971, 2000.

Schubert, G., and D. T. Sandwell, A global survey of possible subduction sites on Venus, *Icarus*, *117*, 173–196, 1995.

Schubert, G., V. S. Solomatov, P. J. Tackley, and D. L. Turcotte, Mantle

convection and the thermal evolution of Venus, in *Venus II*, edited by S. W. Bougher, D. M. Hunten, and R. J. Phillips, pp. 1245–1287, Univ. of Arizona Press, Tucson, 1997.

Schutz, B. E., H. J. Zwally, C. A. Shuman, D. Hancock, and J. P. Di-Marzio, Overview of the ICESat mission, *Geophys. Res. Lett.*, *32*, L21S01, doi:10.1029/2005GL024,009, 2005.

Shuman, C., H. J. Zwally, B. E. Schutz, Z. C. Brenner, J. P. DiMarzio, V. P. Suchdeo, and H. A. Fricker, ICESat Antarctic elevation data: preliminary precission and accuracy assessment, *Geophys. Res. Lett.*, *33*, L07,501, doi:10.1029/2005GL025,227, 2006.

Simons, F. J., M. T. Zuber, and J. Korenaga, Isostatic response of the Australian lithosphere: Estimation of effective elastic thickness and anisotropy using multitaper spectral analysis, *J. Geophys. Res.*, *105*(B8), 19,163–19,184, 2000.

Simons, F. J., R. D. van der Hilst, and M. T. Zuber, Spatio-spectral localization of isostatic coherence anisotropy in Australia and its relation to seismic anisotropy: Implications for lithospheric deformation, *J. Geophys. Res.*, *108*(B5), 2250, doi: 10.1029/2001JB000,704, 2003.

Simons, F. J., F. A. Dahlen, and M. A. Wieczorek, Spatiospectral localization on the sphere, *SIAM Rev.*, *in press*, 2006.

Simons, M., B. H. Hager, and S. C. Solomon, Global variations in the geoid/topography admittance of Venus, *Science*, *264*, 798–803, 1994.

Simons, M., S. C. Solomon, and B. H. Hager, Localization of gravity and topography: Constraints on the tectonics and mantle dynamics of Venus, *Geophys. J. Int.*, *131*, 24–44, 1997.

Sjogren, W. L., W. B. Banerdt, P. W. Chodas, A. S. Konopliv, G. Balmino, J. P. Barriot, T. R. Colvin, M. E. Davies, and J. Arkani-Hamed, The Venus gravity field and other geodetic parameters, in *Venus II*, edited by S. W. Bougher, D. M. Hunten, and R. J. Phillips, pp. 1125–1161, Univ. of Arizona Press, Tucson, 1997.

Slepian, D., Some comments on Fourier-analysis, uncertainty and modeling, *SIAM Rev.*, *25*(3), 379–393, 1983.

Smith, D. E., M. T. Zuber, G. A. Neumann, and F. G. Lemoine, Topography of the moon from clementine lidar, *J. Geophys. Res.*, *102*, 1591–1611, 1997.

Smith, D. E., M. T. Zuber, and G. A. Neumann, Seasonal variations of snow depth on Mars, *Science*, *294*, 2141–2146, 2001a.

Smith, D. E., et al., The global topography of Mars and implications for surface evolution, *Science*, *284*, 1495–1503, 1999.

Smith, D. E., et al., Mars Orbiter Laser Altimeter: Experiment summary after the first year of global mapping of Mars, *J. Geophys. Res.*, *106*(E10), 23,689–23,722, 2001b.

Smith, W. H. F., and D. T. Sandwell, Global sea floor topography from satellite altimetry and ship depth soundings, *Science*, *277*(5334), 1956–1962, 1997.

Smith, W. H. F., and D. W. Sandwell, Bathymetric prediction from dense satellite altimetry and sparse shipboard bathymetry, *J. Geophys. Res.*, *99*, 21,803–21,824, 1994.

Smrekar, S. E., Evidence for active hotspots on Venus from analysis of Magellan gravity data, *Icarus*, *112*, 2–26, 1994.

Smrekar, S. E., and R. J. Phillips, Venusian highlands: geoid to topography ratios and their implications, *Earth Planet. Sci. Lett.*, *107*, 582–597, 1991.

Smrekar, S. E., and E. R. Stofan, Origin of corona-dominated topographic rises on Venus, *Icarus*, *139*, 100–115, 1999.

Smrekar, S. E., R. Comstock, and F. S. Anderson, A gravity survey of type 2 coronae on Venus, *J. Geophys. Res.*, *108*(E8), 5090, doi:10.1029/2002JE001,935, 2003.

Sneeuw, N., Global spherical harmonic-analysis by least-squares and numerical quadrature methods in historical perspective, *Geophys. J. Int.*, *118*(3), 707–716, 1994.

Solomon, S. C., and J. W. Head, Lunar mascon basins: lava filling, tectonics, and evolution of the lithosphere, *Rev. Geophys. Space Phys.*, *18*, 107–141, 1980.

Solomon, S. C., and J. W. Head, Lithospheric flexure beneath the Frejya Montes foredeep, Venus: constraints on lithospheric thermal gradient and heat flow, *Geophys. Res. Lett.*, *17*(9), 1393–1396, 1990.

Sugano, T., and K. Heki, Isostasy of the Moon from high-resolution gravity and topography data: Implication for its thermal history, *Geophys. Res. Lett.*, *31*, L24,703, doi:10.1029/2004GL022,059, 2004.

Tapley, B., et al., GGM02—an improved Earth gravity field model from GRACE, *J. Geodesy*, *79*, doi: 10.1007/s00,190–005–0480–z, 2005.

Tapley, B. D., S. Bettadpur, J. C. Ries, P. F. Thompson, and M. Watkins, GRACE measurements of mass variability in the Earth system, *Science*, *305*, 503–505, 2004.

Thébault, E., J. J. Schott, M. Mandea, and J. P. Hoffbeck, A new proposal for spherical cap harmonic modelling, *Geophys. J. Int.*, *159*, 83–103, 2004.

Thébault, E., J. J. Schott, and M. Mandea, Revised spherical cap harmonic analysis (R-SCHA): validation and properties, *J. Geophys. Res.*, *111*, B01,102, doi:10.1029/2005JB003,836, 2006.

Thomson, D. J., Spectrum estimation and harmonic analysis, *Proc. IEEE*, *70*(9), 1055–1096, 1982.

Toksöz, M. N., A. M. Dainty, S. C. Solomon, and K. R. Anderson, Structure of the moon, *Rev. Geophys.*, *12*, 539–567, 1974.

Turcotte, D. L., How does Venus lose heat?, *J. Geophys. Res.*, *100*(E8), 16,931–16,940, 1995.

Turcotte, D. L., R. J. Willemann, W. F. Haxby, and J. Norberry, Role of membrane stresses in the support of planetary topography, *J. Geophys. Res.*, *86*, 3951–3959, 1981.

U. S. Geological Survey, Color-coded topography and shaded relief map of the lunar near side and far side hemispheres, *I-2769*, 2002.

Varshalovich, D. A., A. N. Moskalev, and V. K. Khersonskii, *Quantum theory of angular momentum*, World Scientific, Singapore, 1988.

Vezolainen, A. V., V. S. Solomatov, A. T. Basilevsky, and J. W. Head, Uplift of Beta Regio: Three-dimensional models, *J. Geophys. Res.*, *109*, E08,007, doi:10.1029/2004JE002,259, 2004.

Watters, T., Lithospheric flexure and the origin of the dichotomy boundary on Mars, *Geology*, *31*, 271–274, 2003.

Watters, T. R., A. C. Cook, and M. S. Robinson, Large-scale lobate scarps in the southern hemisphere of mercury, *Planet. Space Sci.*, *49*, 1523–1530, 2001.

Watters, T. R., R. Schultz, M. S. Robinson, and A. C. Cook, The mechanical and thermal structure of mercury's early lithosphere, *Geophys. Res. Lett.*, p. doi: 10.1029/2001GL014308, 2002.

Watts, A. B., *Isostasy and Flexure of the Lithosphere*, Cambridge Univ. Press, Cambridge, UK, 2001.

Watts, A. B., and E. B. Burov, Lithospheric strength and its relationship to the elastic and seismogenic layer thickness, *Earth Planet. Sci. Lett.*, *213*, 113–131, 2003.

Watts, A. B., and S. Zhong, Observations of flexure and the rheology of oceanic lithosphere, *Geophys. J. Int.*, *142*, 855–875, 2000.

Webb, D. J., Tides and the evolution of the Earth-Moon system, *Geophys. J. R. Astron. Soc.*, *70*, 261–271, 1982.

Werner, R. A., Spherical harmonic coefficients for the potential of a constant-density polyhedron, *Comp. Geosci.*, *23*, 1071–1077, 1997.

Werner, R. A., and D. J. Scheeres, Exterior gravitation of a polyhedron derived and compared with harmonic and mascon gravitation representations of asteroid 4769 Castalia, *Celest. Mech. Dynam. Astron.*, *65*, 313–344, 1997.

Wessel, P., and W. H. F. Smith, Free software helps map and display data, *EOS*, *72*(441), 1991.

Wieczorek, M., and R. J. Phillips, Lunar multiring basins and the cratering process, *Icarus*, *139*, 246–259, 1999.

Wieczorek, M. A., and R. J. Phillips, The structure and compensation of the lunar highland crust, *JGR*, *102*(E5), 10,933–10,943, 1997.

Wieczorek, M. A., and R. J. Phillips, Potential anomalies on a sphere: Applications to the thickness of the lunar crust, *J. Geophys. Res.*, *103*(E1), 1715–1724, 1998.

Wieczorek, M. A., and R. J. Phillips, The "Procellarum KREEP Terrane": Implications for mare volcanism and lunar evolution, *J. Geophys. Res.*, *105*(E8), 20,417–20,430, 2000.

Wieczorek, M. A., and F. J. Simons, Localized spectral analysis on the sphere, *Geophys. J. Int.*, p. in press, 2005.

Wieczorek, M. A., and F. J. Simons, Minimum variance multitaper spectral estimation on the sphere, *J. Fourier Anal. Appl.*, *in press*, 2007.

Wieczorek, M. A., and M. T. Zuber, Thickness of the Martian crust: Improved constraints from geoid-to-topography ratios, *J. Geophys. Res.*, *109*, E01,009, doi:10.1029/2003JE002,153, 2004.

Wieczorek, M. A., et al., The constitution and structure of the lunar interior, in *New views of the Moon*, *Rev. Min. Geochem.*, vol. 60, edited by B. J. Jolliff, M. A. Wieczorek, C. K. Shearer, and C. R. Neal, pp. 221–364, Mineral. Soc. Amer., 2006.

Willemann, R. J., and D. L. Turcotte, Support of topographic and other loads on the moon and on the terrestrial planets, *Proc. Lunar Planet. Sci. Conf.*, *12B*, 837–851, 1981.

Yoder, C. F., Astrometric and geodetic properties of Earth and the solar system, in *Global Earth Physics: A handbook of physical constants*, edited by T. J. Ahrens, AGU reference shelf 1, pp. 1–31, American Geophysical Union, 1995.

Yuan, D. N., W. L. Sjogren, A. S. Konopliv, and A. B. Kucinskas, Gravity field of Mars: A 75th degree and order model, *J. Geophys. Res.*, *106*(E10), 23,377–23,401, 2001.

Zharkov, V. N., V. V. Leontjev, and A. V. Kozenko, Models, figures and gravitational moments of the Galilean satelites of Jupiter and icy satellites of Saturn, *Icarus*, *61*, 92–100, 1985.

Zhong, S., Effects of lithosphere on the long-wavelength gravity anomalies and their implications for the formation of the Tharsis rise on Mars, *J. Geophys. Res.*, *107*(E7), 5054, doi:10.1029/2001JE001,589, 2002.

Zuber, M. T., The crust and mantle of Mars, *Nature*, *412*, 237–244, 2001.

Zuber, M. T., T. D. Bechtel, and D. W. Forsyth, Effective elastic thicknesses of the lithosphere and mechanisms of isostatic compensation in Australia, *J. Geophys. Res.*, *94*(B7), 9353–9367, 1989.

Zuber, M. T., D. E. Smith, F. G. Lemoine, and G. A. Neumann, The shape and internal structure of the Moon from the Clementine mission, *Science*, *266*, 1839–1843, 1994.

Zuber, M. T., et al., Internal structure and early thermal evolution of Mars from Mars Global Surveyor topography and gravity, *Science*, *287*, 1788–1793, 2000a.

Zuber, M. T., et al., The shape of 433 Eros from the NEAR-Shoemaker Laser Rangefinder, *Science*, *289*, 2097–2101, 2000b.

Zuber, M. Y., and D. E. Smith, Mars without Tharsis, *J. Geophys. Res.*, *102*, 28,673–28,685, 1997.